Structure tuning, strong second harmonic generation response, and high optical stability of the polar semiconductors Na_{1-x}K_xAsQ₂

Abishek K. Iyer^a, Jeong Bin Cho^b, Hye Ryung Byun^b, Michael J. Waters^c, Shiqiang Hao^c, Benjamin M. Oxley^a, Venkat Gopalan^d, Christopher Wolverton^c, James M. Rondinelli^c, Joon I. Jang^b and Mercouri G. Kanatzidis^a, *

^aDepartment of Chemistry and Department of Physics and Astronomy, Northwestern University, Evanston, Illinois 60208, and Materials Science Division, Argonne National Laboratory, Argonne, Illinois 60439, USA

^bDepartment of Physics, Sogang University, 35 Baekbeom-ro, Mapo-gu, Seoul 04107, Korea

^cDepartment of Materials Science and Engineering, Northwestern University, Evanston, Illinois 60208, USA

^dDepartment of Materials Science and Engineering, Pennsylvania State University, Pennsylvania, 16802, USA

* Corresponding author

Abstract

The mixed cation compounds $Na_{1-x}K_xAsSe_2$ (x = 0.8, 0.65, 0.5) and $Na_{0.1}K_{0.9}AsS_2$ crystallize in the polar noncentrosymmetric space group Cc. The $AAsQ_2$ (A = alkali metals, Q = S, Se) family features onedimensional (1D) $^{1}/_{\infty}[AQ_{2}^{-}]$ chains comprising corner-sharing pyramidal AQ_{3} units in which the packing of these chains is dependent on the alkali metals. The parallel $\frac{1}{\infty}[AO_2]$ chains interact via short As...Se contacts, which increase in length when the fraction of K atoms is increased. The increase in the As...Se inter-chain distance increases the bandgap from 1.75 eV in γ-NaAsSe₂ to 2.01 eV in Na_{0.35}K_{0.65}AsSe₂, 2.07 eV in $Na_{0.2}K_{0.8}AsSe_2$, and 2.18 eV in $Na_{0.1}K_{0.9}AsS_2$. The $Na_{1-x}K_xAsSe_2$ (x = 0.8, 0.65) compounds melt congruently at approximately 316 °C. Wavelength-dependent second-harmonic generation (SHG) measurements on powder samples of $Na_{1-x}K_xAsSe_2$ (x = 0.8, 0.65, 0.5) and $Na_{0.1}K_{0.9}AsS_2$ suggest that Na_{0.2}K_{0.8}AsSe₂ and Na_{0.1}K_{0.9}AsS₂ have the highest SHG response and exhibit significantly higher laserinduced damage thresholds (LIDTs). Theoretical SHG calculations on Na_{0.5}K_{0.5}AsSe₂ confirm its SHG response with the highest value of $d_{33} = 22.5$ pm/V ($\chi_{333}^{(2)} = 45.0$ pm/V). The effective nonlinearity for randomly oriented powder is calculated to be $d_{\text{eff}} = 18.9 \text{ pm/V}$ ($\chi_{\text{eff}}^{(2)} = 37.8 \text{ pm/V}$), which is consistent with the experimentally obtained value of $d_{\rm eff} = 16.5$ pm/V ($\chi_{\rm eff}^{(2)} = 33.0$ pm/V). Three-photon absorption is the dominant mechanism for the optical breakdown of the compounds under intense excitation levels at 1580 nm with Na_{0.2}K_{0.8}AsSe₂ exhibiting the highest stability.

Key words: chalcogenide, dimensional reduction, chalcoarsenates, nonlinear optics

1. Introduction

In the past decade, there has been a surge in interest in new materials for applications in second-order nonlinear optics in the infrared (IR) region. Chalcogenides offer the strong advantage of being transparent in the IR region, while their structural diversity offers a wide range of materials that can be used in highpower lasers for wavelengths above 2 µm.^{1,2-4} The applications for such wavelengths include the detection of chemical warfare agents,⁵ gas pollutants, and trace gases,⁶ and advanced telecommunications^{7, 8}, for which chalcogenides are fully transparent while many known oxides are not. The current benchmark nonlinear optical (NLO) materials for wavelengths above 2 µm are AgGaS₂, AgGaSe₂, and ZnGeP₂. These materials have high NLO coefficients and wideband IR transparency; however, AgGa $O_2(O = S, Se)$ suffers from a low laser-induced damage threshold (LIDT)⁸ while other materials, such as ZnGeP₂, suffer from the two-photon absorption effect. 9 New compounds with high LIDTs are preferred, even at the expense of the second harmonic generation (SHG) conversion efficiency, because they are more useful for high-power NLO applications. Recent reviews by Chung et al., Liang et al., and Lin et al. offer useful suggestions for the design of new NLO materials through the introduction of main-group element-centered tetrahedra and distorted polyhedra derived from second-order Jahn-Teller distortion and/or stereochemically active lone pairs. Nonetheless, it remains difficult to predict if the incorporation of distorted polyhedra experimentally produces noncentrosymmetric structures (NCSs).¹¹

Previously, we described the alkali metal-containing one-dimensional (1D) materials β-LiAsS₂, which has the maximum $\chi^{(2)}$ component of 196 pm/V, as well as γ -NaAsSe₂, (324.6 pm/V), ¹² KPSe₆ (157 pm/V), ¹³ $K_{0.6}Cs_{0.4}PSe_6$ (163 pm/V), ¹⁴ and RbPSe₆ (149 pm/V), ¹⁵ and the two-dimensional (2D) structures Na₂Ge₂Se₅ (290 pm/V) and Na₂Ge₂Se_{4.55}Te_{0.45} (118 pm/V). ¹⁶ These materials show much higher SHG responses than the benchmark AgGaS₂ (26 pm/V), AgGaSe₂ (66 pm/V) and ZnGeP₂ (150 pm/V).³ The chalcoarsenate system $AAsQ_2$ (A = alkali-metals; Q = S, Se) contains 1D $1/\infty[AQ_2]$ chains that are connected via cornersharing pyramidal AsQ₃ units. 12, 17 The molecular conformation of these chains and the size of the alkali cation strongly affect the bandgap as well as the SHG response of these materials. In LiAsO₂, the smaller Li ions result in a stronger interchain interaction (As···Se), while the substitution of Li by larger Na ions weakens the As...Se interactions, thereby increasing the 1D character of the system. The increase in the interchain distance results in a significant increase in the bandgap and SHG intensities. β-LiAsS₂ exhibits a SHG signal 10 times that of AgGaSe₂¹⁷ while the SHG signal in γ-NaAsSe₂ is 75 times that of AgGaSe₂. 12 It was also observed that when Na was added to LiAsSe₂, the resulting compounds β-Li_{0.2}Na_{0.8}AsSe₂ and γ-Li_{0.2}Na_{0.8}AsSe₂ exhibited strong SHG signals that are approximately 55 and 65 times that exhibited by AgGaSe₂, respectively. ¹² Noncentrosymmetric structures were observed in the sulfides Li_{1-x}Na_xAsS₂ up to x = 0.4 with $Li_{0.6}Na_{0.4}AsS_2$ having a SHG response 30 times that of AgGaSe₂. This is higher than the SHG

response of LiAsS₂, which is only 10 times that of AgGaSe₂.¹⁷ These results do not follow the expected norm wherein the SHG intensity decreases with increasing bandgap. ^{18, 19} Cation substitution with Cs in the KPSe₆ systems, which also contains $1D^{-1}/_{\infty}[PSe_6^{-1}]$ chains, resulted in very little changes in the interchain distance, bandgap, and SHG response¹⁴. Theoretical studies predicted a χ^2 of 324 pm/V¹⁵ in γ-NaAsSe₂ and $d_{33} = 836.5$ pm/V in β-LiAsSe₂²⁰, which is the highest value among mid-IR SHG materials. Despite these high SHG intensities, γ-NaAsSe₂ suffers from a polymorphic phase transition to centrosymmetric δ-NaAsSe₂ upon cooling from the melt, which makes it difficult to grow large single crystals. The bandgap of β-LiAsSe₂ is 1.11 eV, suggesting that it may have a low LIDT. ^{10, 12} Li_{0.6}Na_{0.4}AsS₂ melts incongruently while γ-Li_{0.2}Na_{0.8}AsSe₂ undergoes a phase transition to β-Li_{0.2}Na_{0.8}AsSe₂. ¹² The effect of cation substitution in these quasi-1D systems on their optical bandgap and the SHG response offers an avenue for understanding the relationships between their optical properties and their structures in a systematic manner, which can ultimately lead to the rational design of new NLO materials.

Motivated by these results, we report on the effects of K cation substitution into the γ -NaAsSe₂ structure. We found that Na_{1-x}K_xAsSe₂ (x = 0.8, 0.65, 0.5) and Na_{0.1}K_{0.9}AsS₂ crystallize in a new noncentrosymmetric structure, and that the $^{1}/_{\infty}[AQ_{2}^{-}]$ chains have a new molecular conformation and a much larger interchain distance compared to β-LiAsSe₂ and γ -NaAsSe₂. The bandgaps of these compounds are larger than those of γ -NaAsSe₂ and β-LiAsSe₂. The large bandgaps can be explained by a decrease in the valence bandwidth. The As^{...}Se interchain interactions are weaker than the parent γ -NaAsSe₂ which decreases the melting and crystallization temperatures of these materials. We found that Na_{1-x}K_xAsSe₂ (x = 0.8, 0.65, 0.5) and Na_{0.1}K_{0.9}AsS₂ have comparable SHG responses to that of AgGaSe₂, but higher LIDTs than γ -NaAsSe₂

2. Experimental Section

Starting materials. All manipulations were performed under a dry nitrogen atmosphere in a glove box. Commercially available potassium (K, Sigma Aldrich, 99.95%), sodium (Na, Sigma Aldrich, 99.5%), arsenic (As, Alfa Aesar, 99.9%), and selenium (Se, American elements, 99.999%) were used without further purification. Li₂Se, Na₂Se, K₂Se, and K₂S were prepared by a modified literature procedure by reacting the alkali metals and selenium in liquid ammonia^{21, 22} Warning: Elemental arsenic was weighed out in the glovebox. Precautions must be taken in preparing these samples because of their high toxicity.

2.1 Synthesis of Na_{0.2}K_{0.8}AsSe₂

A mixture of 0.233 g of K_2Se (1.4 mmol), 0.046 g of Na_2Se (0.3 mmol), 0.278 g of As (3.7 mmol), and 0.440 g of Se (5.5 mmol) was ground and loaded in a separate carbon-coated fused silica tube (13 mm OD, 11 mm ID) inside a nitrogen-filled glovebox. The tube was then flame-sealed under vacuum (approximately 3×10^{-3} mbar) and inserted into a programmable tube furnace. The temperature was increased to 500 °C

over 10 h. The sample was annealed at 500 °C for 48 h, and then cooled to 250 °C over 96 h. The furnace was then shut off to obtain the product. Semi-quantitative energy dispersive analysis using scanning electron microscopy (SEM/EDX) confirmed the composition and the spectrum can be found in Figure S1(a). The detailed synthesis of all the other compounds is provided in the Supporting Information (SI).

All compounds were stored in a glovebox because their surfaces started to darken after exposure to ambient conditions for more than 2 h. The powder XRD patterns of these samples remained unaffected, but the bandgap decreased substantially as described in the SI. Table 1 shows the crystallographic data for Na_{0.2}K_{0.8}AsSe₂, Na_{0.35}K_{0.65}AsSe₂, Na_{0.5}K_{0.5}AsSe₂ and Na_{0.1}K_{0.9}AsS₂.

The solvent stability and solubility of $Na_{0.2}K_{0.8}AsSe_2$ and $Na_{0.35}K_{0.65}AsSe_2$ in water, anhydrous acetone, methanol, hexane, and hydrazine were investigated. Both compounds degraded in water, and additional diffraction peaks were observed after an hour in anhydrous methanol and acetone, as shown in Figure S2a of the SI. The compounds were unaffected by hexane. Similar to γ -NaAsSe₂, these compounds readily dissolved in anhydrous hydrazine to form bright orange solutions (Figure S2b). The solutions remained orange for more than a month.

2.2 Theoretical SHG calculations

Ground state calculations were also performed with VASP and employed the electronic convergence criterion of 10⁻⁸ eV total energy change between electronic iterations.²³ Structural relaxation without any symmetry constraints were terminated when no forces exceeded 0.5 meV/Å. The plane wave energy cutoff was 550 eV, and the augmentation grid cutoff was 2200 eV. Structures were resymmetrized to the closest space group and re-relaxed to confirm the space group assignments. The Brillouin zones were sampled with k-point grids ensuring a minimum density of 50,000 k-points per reciprocal Å³. The pseudopotentials included in VASP were used in this study. Abinit version 9.2.2 was used for calculating the linear and nonlinear optical properties.²⁴ Simulation preparation and post-processing were performed with Atomic Simulation Environment (ASE) version 3.19.1.²⁵ Single-point calculations were performed with Abinit within a single particle approximation using the Abinit utility Optic before the optical property calculations. Convergence was satisfied in the electronic solver when there was no energy eigenvalue change of more than 10⁻⁵ eV between steps. The plane wave cutoff was 400 eV, and the augmentation grid cutoff was set to 600 eV. The pseudopotentials used were obtained from the standard accuracy set of ATOMPAW version 4.0.0.12.26 The number of empty bands was increased until the highest empty band was 20 eV above the valence band maximum. The optical properties were calculated with 50 meV broadening and with scissor shifts to compensate for the difference between the DFT fundamental gap and the herein experimentally measured bandgap.

2.3 Nonlinear optical measurements

Crystalline powders of $Na_{0.2}K_{0.8}AsSe_2$, $Na_{0.35}K_{0.65}AsSe_2$, $Na_{0.5}K_{0.5}AsSe_2$, and $Na_{0.1}K_{0.9}AsS_2$ with the size ranges of <25 µm, 25–53 µm, 53–75 µm, 75–106 µm, 106–150 µm, and >150 µm after sieving were used for SHG measurements to examine the phase-matching behavior, LIDT, and wavelength-dependent SHG of the samples. To prevent moisture from affecting the samples, each sample was sieved inside a glovebox, flame sealed in a glass capillary tube, and mounted on a homemade sample holder. The SHG responses of the samples were compared with those of the benchmark reference material, $AgGaSe_2$.

The SHG measurements were carried out at room temperature using input wavelengths λ ranging from 1200 to 2000 nm maintained at the same intensity (89 MW/cm²), except for γ-NaAsSe₂ (24 MW/cm²), which exhibited a high SHG response. We confirmed that the sample damage at this intensity was insignificant. Coherent light with the wavelength of 1064 nm for the generation of tunable pulses was initially produced using an EKSPLA PL-2250 series diode-pumped Nd:YAG laser with the pulse width of 30 ps and repetition rate of 50 Hz. The Nd:YAG laser pumped an EKSPLA Harmonics Unit (HU) H400, in which the input beam was frequency tripled by a cascade of NLO beam mixing. The 355 nm beam then entered an EKSPLA PG403-SH-DFG optical parametric oscillator (OPO) composed of four main parts: (i) a double-pass parametric generator, (ii) a single-pass parametric amplifier, (iii) a second-harmonic generator, and (iv) a difference frequency generation (DFG) scheme. The input beam was focused onto the sample using a lens (f = 75 mm). The SHG signal was collected using a collection lens system under a reflection geometry and transmitted through a fiber-optic bundle to a spectrometer equipped with a CCD camera. The data was collected for 20 s. The spot size was 300 µm in diameter. The reason for this big spot size is to cover a large area to average the randomness of powders. Detailed descriptions of our laser and detection setup can be found elsewhere.²⁷ The output wavelength of the OPO used in our experiments was varied from 1200 nm to 2000 nm in increments of 100 nm for wavelength-dependent SHG. Therefore, the corresponding SHG wavelength range was $\lambda_{SHG} = \lambda/2 = 600 - 1000$ nm. For the assessment of the second-order susceptibility, $\chi^{(2)}$, λ was tuned to 1580 nm, which was deliberately selected to ensure that SHG ($\lambda_{SHG} = 790$ nm) occurred below the bandgap of both the test and the reference samples. This implies that the effect of two-photon absorption (2PA) could be neglected in our measurements.

3. Results and Discussion

3.1 Synthesis of $Na_{1-x}K_xAsSe_2$ and $Na_{0.1}K_{0.9}AsS_2$

Na_{0.2}K_{0.8}AsSe₂, Na_{0.35}K_{0.65}AsSe₂, and Na_{0.1}K_{0.9}AsS₂ were obtained in quantitative yield and in pure form (Figure 1a, Figure S5a). They are isostructural to the low-temperature phase of KAsSe₂, as shown in the

representative powder XRD patterns in Figure 1a. Sheldrick *et al.* reported the synthesis of crystalline KAsSe₂ via a low-temperature (130 °C) solvothermal reaction.²⁸ Our attempts to prepare KAsSe₂ and KAsS₂ with solid-state methods at high temperatures (500 °C), however, surprisingly yielded air- and moisture-sensitive amorphous glassy products (Figure S3b). Evidently, KAsQ₂ is an excellent glass former when cooled from the melt in a manner similar to silica (SiO₂), which can only be crystallized under hydrothermal conditions. Similar difficulties were encountered in obtaining homogeneous and highly crystalline phases of the K-rich compositions Na_{0.2}K_{0.8}AsSe₂ and Na_{0.1}K_{0.9}AsS₂. Slow cooling of the reaction mixture over 96 h (2.6°C/h) was necessary to yield homogeneous and crystalline Na_{0.2}K_{0.8}AsSe₂ (Figure 1a) and Na_{0.1}K_{0.9}AsS₂ (Figure S5c). An amorphous product was obtained for Na_{0.2}K_{0.8}AsSe₂ when the molten reaction mixture was air-quenched, as shown in the diffraction pattern in Figure S3a. The cooling rate of 2.6 °C/h was thus the preferred rate for the synthesis of Na_{0.35}K_{0.65}AsSe₂. The phase purity and the cell constants (Table S16) obtained from the experimental powder refinements (Figure S4) to confirm sample homogeneity.

The noncentrosymmetric $Na_{0.5}K_{0.5}AsSe_2$ phase was always accompanied by the centrosymmetric polymorph of the δ -NaAsSe₂-type structure, irrespective of the temperature profile used (Figure S5a). The best results yielded 91% noncentrosymmetric $Na_{0.5}K_{0.5}AsSe_2$ and 9% δ -Na_{0.5}K_{0.5}AsSe₂ phases. The effect of the latter phase on the experimental SHG counts is within the typical uncertainty rage of the powder method. The unit cell volumes are compared for different compositions of the $Na_{1-x}K_xAsSe_2$ samples in Figure 1b. The unit cell volume decreased with decreasing K fraction in the structure. For the Na-rich phases $Na_{0.6}K_{0.4}AsSe_2$ and $Na_{0.8}K_{0.2}AsSe_2$, the change in the unit cell volume was negligible. Attempts to prepare $Li_{1-x}K_xAsSe_2$ compositions yielded a mixture of β -LiAsSe₂ and amorphous KAsSe₂. The powder XRD of the attempted $Li_{0.8}K_{0.2}AsSe_2$ phase contained Bragg peaks belonging to β -LiAsSe₂ (Figure S6a). Even when the molten " $Li_{0.8}K_{0.2}AsSe_2$ " was air-quenched, the resulting solid was a mixture of two phases, α -LiAsSe₂ and β -LiAsSe₂, as shown in Figure S6b. Several other heating profiles were attempted for the formation of $Li_{0.8}K_{0.2}AsSe_2$ but they did not succeed. The EDS analysis of the crystals obtained from these reactions did not suggest the presence of K. K was found in the amorphous part of the sample, which consisted of KAsSe₂, as mentioned above.

The NaAsSe₂ composition has two polymorphs: noncentrosymmetric γ -NaAsSe₂¹² and centrosymmetric δ -NaAsSe₂²⁹ while the composition of LiAsSe₂ comprises centrosymmetric α -LiAsSe₂ and noncentrosymmetric β -LiAsSe₂. The centrosymmetric structures α -LiAsSe₂ and δ -NaAsSe₂ were obtained by air quenching the reaction mixture at 500 °C. 12

3.2 Structure comparison across the different $AAsSe_2$ phases (A = Li, Na and K)

The crystal structure of Na_{1-x}K _xAsSe₂ (x = 0.8, 0.65, 0.5) belongs to the KAsSe₂-type structure reported by Sheldrick *et al.*²⁸ The structure was initially reported as triclinic P1, but Kapon *et al.* suggested a higher symmetry monoclinic space group Cc.³⁰ To understand the important effect of the alkali cation on the interchain interactions, we compare the structures of β -LiAsSe₂, γ -NaAsSe₂, and Na_{0.2}K_{0.8}AsSe₂. All phases contain infinite 1D $^{1}/_{\infty}[AQ_{2}^{-}]$ chains, which are defined by corner sharing of the AsSe₃ units (Figure 2); however, these phases are distinguished by the conformation of the chains and the direction along which the chains propagate.

The chains in Na_{0.2}K_{0.8}AsSe₂ are made up of distorted corner-sharing AsSe₃ trigonal pyramids containing two As-Se_b (b = bridging) bonds (2.45 and 2.42 Å), which are longer than the As-Se_t (t = terminal) bond (2.30 Å). This is similar to LiAsSe₂ (As-Se_b = 2.46 Å, 2.47 Å; As-Se_t = 2.32 Å) and γ -NaAsSe₂ (As-Se_b = 2.51 Å, 2.46 Å; As-Se_t = 2.34 Å), as shown in Figure S7. The conformation can be understood from the repeating number of the AsSe₃ linkages (highlighted using a dashed square in Figure 2a, 2b, 2c). In β -LiAsSe₂, the chain has a repeating unit consisting of two differently linked AsSe₃ or *zweier* chains (Figure 2a), while γ -NaAsSe₂ (Figure 2b) and KAsSe₂ (Figure 2c) have four differently linked AsSe₃ units or *vierer* chains. The chain conformations of γ -NaAsSe₂ and Na_{0.2} K_{0.8}AsSe₂ are completely different. In γ -NaAsSe₂, three of the AsSe₃ units point in the same direction and the fourth unit is twisted with an As-Se-As angle of 95.168°, while in Na_{0.2} K_{0.8}AsSe₂, all the AsSe₃ units are tilted with As-Se-As angles of 97° and 94.6°. The 1D chains are aligned along the *a*-axis in β -LiAsSe₂ (Figure S7a) and along the *b*-axis in γ -NaAsSe₂ (Figure S7b), but grow on the *ac*-plane in Na_{1-x}K_xAsSe₂ (x = 0.8, 0.65, 0.5) (Figure S7c). The conformations are clearly dependent on the size and coordination environment of the alkali-metal cation.

The increase in ionic radius from Li (90 pm) to Na (112 pm) and K (180 pm)³¹ strongly affects the secondary As···Se interactions between adjacent $^{1}/_{\infty}[AQ^{2^{-}}]$ chains, as illustrated in Figure S8. The graph in Figure 3 shows the interchain distances, which are defined as the distance between the nearest As···Se. The interchain distance is 3.37 Å in β -LiAsSe₂, increases to 3.62 Å in γ -NaAsSe₂, and further increases to 4.29 Å in Na_{0.2}K_{0.8}AsSe₂. Figure 4a, 4b, and 4c show the increase in interchain distances with the increase in the amount of K in the Na_{1-x}K _xAsSe₂ (x = 0.8, 0.65, 0.5) structures. The shortest As···Se distance is 3.99 Å in Na_{0.5}K_{0.5}AsSe₂ and the longest interchain distance is 4.41 Å in Na_{0.2}K_{0.8}AsSe₂. Na_{0.1}K_{0.9}AsS₂ is the only sulfide composition in this phase that crystallizes in the KAsSe₂ structure and has the longest interchain distance of 4.37 Å and shortest interchain distance of 4.01 Å, as shown in Figure 4d.

It is important to note that in Na_{0.5}K_{0.5}AsSe₂, the Na and K atoms have independent unique lattice sites. The unit cell of Na_{0.5}K_{0.5}AsSe₂ is shown in Figure 5a, which shows the two independent sites for K and Na in the structure. The possibility of site mixing between K and Na was checked by refining their occupancy, which was found to be greater than 99% in each site. Both sites had reasonable isotropic atomic

displacement parameter U_{iso} values of 0.03244 Å and 0.03416 Å. When the sites were interchanged, the U_{iso} values increased to 0.0532 Å for the Na site and 0.05762 Å for the K site, suggesting a possibly incorrect assignment of the atoms or partial occupancy of the site. Refinement of the occupancy did not improve the refinement suggesting that there was no site mixing of K and Na. Figure 5b shows the orientation of the 1D chains that propagate on the *ac* plane or along the ($\bar{1}11$) plane, and Figure 5c shows the bond lengths of KSe₆ and NaSe₆ in the distorted octahedra. Table 2 shows the atomic coordinates of Na_{0.5}K_{0.5}AsSe₂. A similar refinement strategy was used to refine Na_{0.35}K_{0.65}AsSe₂, Na_{0.2}K_{0.8}AsSe₂, and Na_{0.1}K_{0.9}AsS₂. Na/K site mixing was observed at only one site in Na_{0.1}K_{0.9}AsS₂. The bond lengths of KSe₆ and (Na/K)Se₆ in Na_{0.2}K_{0.8}AsSe₂ are shown in Figure S9a. The bond lengths of the NaSe₆ octahedra in Na_{0.5}K_{0.5}AsSe₂ (Figure S9b). The distortion parameter ($\Delta d = (1/6) \Sigma [(d_n - d)/d]^2$ in the KSe₆ octahedra (Na_{0.5}K_{0.5}AsSe₂) (0.036 Å) is larger than that of the NaSe₆ octahedra (0.020 Å) of γ-NaAsSe₂. The increased distortion in the Na_{1-x}K_xAsSe₂ compounds plays a role in the freedom of rotation in the $^{1/}$ _∞[AQ_2^{-1}] chains to change their conformation.

The possible formation of $Li_{0.5}K_{0.5}AsSe_2$ in the β-LiAsSe₂ and KAsSe₂ structure types was studied using first-principles DFT calculations where the changes in relative internal energies at 0K were calculated. Since vibrational energies are typically on the order of 1/2kT per degree of freedom, thermally accessible phases typically need to be less than kT/atom in energy above the lowest energy structure. Figure 6 shows that the formation energies of $Li_{0.5}K_{0.5}AsSe_2$ in both the LiAsSe₂ or KAsSe₂ structure types are more than 30 meV/atom above those of the β-LiAsSe₂ and KAsSe₂ phases. This is consistent with the experimental results that Li substitution in KAsSe₂ and K substitution in β-LiAsSe₂ was highly unlikely although a $Li_{0.5}K_{0.5}AsSe_2$ phase may possibly be obtained under kinetic control at low temperatures using solvothermal reactions. Figure 6 also suggests that the substitution of K in β-LiAsSe₂ is unlikely (E_{diff} = +15 meV/atom).

3.3 Differential thermal analysis

Differential thermal analysis (DTA) performed on $Na_{1-x}K_xAsSe_2$ (x = 0.8, 0.65, and 0.5) and $Na_{0.1}K_{0.9}AsS_2$ suggests that the crystallization temperature (T_c) increased with decreasing K content from 264 °C in $Na_{0.2}K_{0.8}AsSe_2$ (Figure 7a) to 271 °C in $Na_{0.35}K_{0.65}AsSe_2$ (Figure 7b) to 287 °C in $Na_{0.5}K_{0.5}AsSe_2$ (Figure S11a). Both phases had a similar melting point (T_m) of approximately 316 °C, with no additional exothermic peaks observed. In the $Na_{0.2}K_{0.8}AsSe_2$ samples, which were obtained by cooling the reaction over 24 h, a glassy phase was formed when the sample was melted and then cooled during the DTA cycle. The powder X-ray diffraction results suggest that no polymorphic conversion occurred in the two compounds (Figure S10 a, b). This was also confirmed by melting the as-synthesized sample and cooling it to room temperature over 96 h, wherein the powder diffraction patterns after the melting and cooling were unchanged from the patterns before. Compared to β -LiAsSe₂ ($T_m = 523$ °C, $T_c = 515$ °C) and γ -NaAsSe₂ ($T_m = 435$ °C, $T_c = 413$

°C)¹⁸, the Na_{1-x}K_xAsSe₂ compounds showed much lower melting and crystallization temperatures. The decreased melting point of Na_{1-x}K _xAsSe₂ compared to β-LiAsSe₂ provides further evidence for the weakening of the interchain interactions by larger alkali ions and the resulting reduction of the lattice cohesion. The DTA of Na_{0.5}K_{0.5}AsSe₂ showed only one exothermic peak (287 °C) and one endothermic peak (318 °C). As mentioned above, however, there were two phases observed in the powder XRD patterns, namely, noncentrosymmetric and centrosymmetric Na_{0.5}K_{0.5}AsSe₂ (see Figure S11a and S11c). Na_{0.1}K_{0.9}AsS₂ exhibited only exothermic peaks at 277 °C and 362 °C, but no crystallization temperature upon cooling, suggesting that the rate of cooling (10 °C/min) could be too fast (Figure S11b and S11d).

3.4 Optical Properties and Theoretical Calculations

Song *et al.* have previously studied the electronic structures of LiAsS₂ and γ -NaAsSe₂, and showed that the quasi-1D structure of γ -NaAsSe₂ provides a high density of states in the valence band. The valence band maximum (VBM) of γ -NaAsSe₂ has a large contribution from the Se p states and a much smaller contribution from the As s and p states, suggesting partial ionicity. However, the conduction band (CB) is dominated by arsenic p states. Additionally, the valence bands (VBs) of γ -NaAsSe₂ are much flatter and have a smaller bandwidth than those of LiAsS₂, thereby suggesting a greater anisotropic character of the 1D chains. The combination of flat bands along the direction of the 1D chains and high density of states is attributed to the large $\chi^{(2)}$ values of γ -NaAsSe₂. Figure 8a shows the calculated electronic band structure of Na_{0.5}K_{0.5}AsSe₂, which has a flat VB similar to that of γ -NaAsSe₂, which is derived from the Se p states (Figure 8b). Similar electronic band structure can be found in KAsSe₂ itself (Figure 8c, 8d). This suggests an increased anisotropy in the 1D chains, which is related to the increased interchain distance in the Na_{1-x}K_xAsSe₂ structures. The CB is derived by arsenic p states, similar to LiAsS₂ and γ -NaAsSe₂.

For comparison, Table 4 shows the calculated effective masses of electrons and holes along the reciprocal directions a^* , b^* , and c^* for KAsSe₂, Na_{0.25}K_{0.75}AsSe₂, Na_{0.5}K_{0.5}AsSe₂, and γ -NaAsSe₂. The effective masses of the electrons (4.96 m₀) and holes (2.37 m₀) are the highest along the c^* direction, which corresponds to the interchain direction in the compound, and smallest along the a^* direction ($m_e = 0.219$ m₀ and m_h = 1.360 m₀). In comparison, the effective masses of KAsSe₂, Na_{0.25}K_{0.75}AsSe₂, and Na_{0.5}K_{0.5}AsSe₂ are much smaller in all directions, indicating that γ -NaAsSe₂ has flatter bands compared to KAsSe₂ and its analogous compounds. This suggests that γ -NaAsSe₂ exhibits greater anisotropy. Among KAsSe₂ and derived compounds, the increase in the effective mass of holes from 0.820 m₀ in KAsSe₂ to 0.880 m₀ in Na_{0.25}K_{0.75}AsSe₂ and 0.890 m₀ in Na_{0.5}K_{0.5}AsSe₂ reflects the slight increase in the flatness of the valence bands along the a^* direction with decreasing fraction of K atoms in the structure. Comparatively, the bands in the VB are broader in the b^* direction and have lower effective masses of 0.52 m₀ in KAsSe₂ and 0.55 m₀ in Na_{0.5}K_{0.5}AsSe₂. The bandwidth of the CB is broader in Na_{0.5}K_{0.5}AsSe₂

compared to that of KAsSe₂ and has a large spatial overlap along the c* direction, as shown by the decreased effective mass of the electron from 0.23 m_0 in the latter to 0.20 m_0 in the former. Brehm *et al.* suggested that because β -LiAsSe₂ has a much smaller hole and electron effective mass compared to γ -NaAsSe₂, it produces more current under illumination.³³

The bandgaps determined from the optical absorption spectra were 2.07 eV for Na_{0.2}K_{0.8}AsSe₂ and 2.01 eV for Na_{0.35}K_{0.65}AsSe₂, which are significantly larger than that of γ-NaAsSe₂ (1.75 eV), as shown in Figure 9a. The band structure shows that the conduction band minimum (CBM) is located between the I and X points of the Brillouin zone in Na_{0.5}K_{0.5}AsSe₂, while the VBM is at X, suggesting that the material has an indirect bandgap of 1.3 eV. The emphasis here is on the trends exhibited by the calculated bandgaps rather than their absolute values because the semilocal DFT functional PBE tends to underestimate the bandgaps relative to the experimentally obtained bandgaps.³⁴ For comparison, KAsSe₂ (Figure 8c) has a theoretical bandgap of 1.5 eV. It has an indirect bandgap with a VBM between X and Γ and a CBM between I and X. The experimental bandgap of this material is unknown, and as mentioned above, the material can be obtained only via solvothermal reactions. The band structure suggests that all the compounds that crystallize in the KAsSe₂ structure have indirect bandgaps. Figure S12a and S12b show the band structure of Na_{0.25}K_{0.75}AsSe₂, which also has an indirect theoretical bandgap of 1.4 eV. The indirect bandgap can be inferred from the broad nature of the experimental optical absorption edges observed for Na_{0.2}K_{0.8}AsSe₂ and Na_{0.35}K_{0.65}AsSe₂ (Figure 9a). The experimental bandgaps obtained for γ-NaAsSe₂ and LiAsS₂ showed sharp band edges with no tails, which is consistent with direct bandgaps as confirmed by band structure calculations. The Tauc method³⁵ was used to fit the experimental data to obtain the bandgaps for semiconductors with direct and indirect optical absorption processes. Because we calculated Na_{0.5}K_{0.5}AsSe₂ and $Na_{0.25}K_{0.75}AsSe_2$ to have indirect bandgaps, Tauc plots of $(\alpha/S)^{1/2}$ vs E (eV) were made for Na_{0.2}K_{0.8}AsSe₂ and Na_{0.35}K_{0.65}AsSe₂ and we obtained bandgaps of 2.07 eV and 2.01 eV, respectively, as shown in Figure S13a. In comparison, for γ -NaAsSe₂, which has a direct bandgap, the Tauc plot of $(\alpha/S)^2$ vs E (eV) gave the bandgap of 1.87 eV (Figure S13b).

Figure 9b shows an increasing trend in the bandgaps for both the selenides (red line) and sulfides (green line) as A in the $AAsQ_2$ family changes from Li to K. In the selenides (red line), the bandgap increases with increasing substitution of Na in LiAsSe₂ from 1.11 eV in LiAsSe₂ to 1.75 eV in the fully substituted γ -NaAsSe₂. This trend of increasing bandgap continues as larger K cations were added to NaAsSe₂. The green line in Figure 9b shows a similar trend for the sulfides, with LiAsS₂ having a bandgap of 1.60 eV and Na_{0.1}K_{0.9}AsS₂ a bandgap of 2.18 eV, as shown in Figure S15b. As the alkali cation gets larger in size the distances between the (1D) $^{1}/_{\infty}[AQ_2^{-1}]$ chains become longer and the interact less with weaker $A\cdots O$

interchain bonding. This results in less orbital overlap and lowers the overall dimensionality of the structure thereby making the energy bands less dispersed resulting in an increase in the bandgap.

Because the samples were found to be sensitive to air and water, freshly prepared samples must be used for these measurements. This could be readily accomplished by covering the sample holder with saran wrap inside a glovebox. Bandgap measurements were also performed without the saran wrap so that the samples were exposed to air and monitored over the course of an hour. The bandgaps changed continuously with time, as shown in Figure S12a, b. The bandgap of Na_{0.2}K_{0.8}AsSe₂ decreased towards the smaller value of 1.67 eV from its original value of 2.07 eV (Figure S14a). During this time, the powder XRD pattern of the sample did not change even when the ground sample was kept in air for 2 h (Figure S14b). The change in bandgap is attributed to the formation of a thin layer of Se, which has a bandgap is 1.67 eV, due to surface oxidation.³⁶ This dramatic change could be seen in the optical diffuse reflectance spectra because optical diffuse reflectance spectroscopy is a surface-sensitive technique, whereas XRD probes the entire bulk sample. The Na_{0.5}K_{0.5}AsSe₂ and Na_{0.6}K_{0.4}AsSe₂ samples were a mixture of both centrosymmetric and noncentrosymmetric structures, which made it difficult to determine the exact bandgap (Figure S15a). The Na_{0.8}K_{0.2}AsSe₂ composition had a bandgap of 1.71 eV, similar to δ-NaAsSe₂ (Figure S15a).

3.4.2 Nonlinear optical measurements

The SHG responses were measured as a function of wavelength for the particle size range of 25–53 μ m in all the samples by varying the fundamental wavelength λ from 1200 nm to 2000 nm as shown in Figure 10. The SHG response of bulk powder materials become weaker when λ_{SHG} approaches the bandgap wavelength of the material a trend which has been demonstrated previously.^{37, 38} This occurs not only because of the strong absorption of the second harmonic light by the material, but also because of the two-photon absorption (2PA) of the fundamental light. The experimental NLO results for polycrystalline samples of Na_{0.2}K_{0.8}AsSe₂, Na_{0.35}K_{0.65}AsSe₂, Na_{0.5}K_{0.5}AsSe₂, and Na_{0.1}K_{0.9}AsS₂, as well as those of AgGaSe₂ and γ -NaAsSe₂ for comparison, are shown in Figure S16 (a–f). In addition, the SHG response for all the compounds is shown as a function of particle size at λ = 1580 nm. The samples appeared to be non-phase matchable with different coherence lengths ranging from <25 μ m to 25–53 μ m.³⁹ The monotonic decrease in the SHG response as the particle size increased suggests that the coherence length was smaller than 20 μ m for AgGaSe₂, Na_{0.1}K_{0.9}AsS₂, and γ -NaAsSe₂. The coherence lengths of Na_{0.2}K_{0.8}AsSe₂, Na_{0.35}K_{0.65}AsSe₂, and Na_{0.5}K_{0.65}AsSe₂ were 39±14 μ m. Using the Kurtz powder method, ⁴⁰ χ ⁽²⁾_{Seff} of each sample was compared with that of χ ⁽²⁾_{Reff} and the reference and estimated using the following formula:

$$\chi_{S_{\text{eff}}}^{(2)} = \chi_{R_{\text{eff}}}^{(2)} \frac{l_R}{l_S} \left(\frac{l_S^{SHG}}{l_S^{SHG}} \right)^{1/2},$$
(1)

where I_s^{SHG} and I_R^{SHG} are the experimentally measured SHG counts and I_S and I_R are the coherence lengths of the sample and the reference, respectively. We calculated the coherence length of AgGaSe₂, $I_R = \lambda/(4\Delta n)$, to be approximately 13.7 μm using the index mismatch at 1580 nm. Assuming the coherence lengths of γ-NaAsSe₂ and Na_{0.1}K_{0.9}AsS₂ to be nearly equal to I_R given their similar bandgaps,⁴¹ we can compare the $\chi_{S_{\rm eff}}^{(2)}$ values of the samples with that of AgGaSe₂. Here we emphasize that both $\chi_{S_{\rm eff}}^{(2)}$ and $\chi_{R_{\rm eff}}^{(2)}$ are the effective values averaged over the random orientation of the powders (see SI for details). Using $\chi_{R_{\rm eff}}^{(2)} \sim 56$ pm/V for AgGaSe₂ (see SI),⁴² we estimated $\chi_{\rm eff}^{(2)}$ [γ-NaAsSe₂] $\sim 148\pm11$ pm/V, $\chi_{\rm eff}^{(2)}$ [Na_{0.5}K_{0.5}AsSe₂] $\sim 33\pm4$ pm/V, $\chi_{\rm eff}^{(2)}$ [Na_{0.35}K_{0.65}AsSe₂] $\sim 28\pm2$ pm/V, $\chi_{\rm eff}^{(2)}$ [Na_{0.2}K_{0.8}AsSe₂] $\sim 37\pm3$ pm/V, and $\chi_{\rm eff}^{(2)}$ [Na_{0.1}K_{0.9}AsS₂] $\sim 38\pm4$ pm/V. The obtained $\chi_{\rm eff}^{(2)}$ values of the compounds are smaller than that of AgGaSe₂ even though the SHG counts (Figure S16) are higher as the coherence lengths of the compounds (I_s) are 3 times that of AgGaSe₂ (I_R). The obtained $\chi_{\rm eff}^{(2)}$ value of γ-NaAsSe₂ is lower than previously reported, which might be due to the air sensitivity of the compounds. As mentioned above, Na_{0.5}K_{0.5}AsSe₂ was found to contain a small fraction of the centrosymmetric δ-Na_{0.5}K_{0.5}AsSe₂ phase which could affect the SHG response but we found negligible variation in the SHG counts when scanned over various locations of the sample.

The theoretical static SHG value in γ-NaAsSe₂ was reported to be dominated by d_{33} = 162.3 pm/V ($\chi_{333}^{(2)}$ = 324.6 pm/V), which corresponds to the direction of chain growth along the *a*-axis. ¹⁵ First-principles SHG calculations on Na_{0.5}K_{0.5}AsSe₂ were performed to confirm the powder SHG response obtained experimentally. Under the restriction of Kleinman symmetry for the point group *m* (space group: *Cc*), there are 10 non-zero SHG tensors d_{11} , d_{12} , d_{13} , d_{15} , d_{24} , d_{26} , d_{31} , d_{32} , d_{33} , and d_{35} (Table S17). The largest static SHG tensor for Na_{0.5}K_{0.5}AsSe₂ is d_{33} = 22.50 pm/V. However, the other tensor values are similar, as can be seen from d_{13} = d_{35} = 16.40 pm/V, d_{15} = d_{31} = -11.99 pm/V, and d_{24} = d_{32} = -13.85 pm/V. In order to directly compare with the experimental value, the theoretical d_{eff} = $\chi_{\text{eff}}^{(2)}$ /2 was calculated to be 18.9 pm/V ($\chi_{\text{eff}}^{(2)}$ = 37.8 pm/V), which is consistent with the experimentally obtained value of d_{eff} = 16.5 pm/V ($\chi_{\text{eff}}^{(2)}$ = 33.0 pm/V). Figure 11(a) shows that the $\chi_{\text{eff}}^{(2)}$ values of all these compositions remained high; however, it was not significantly enhanced by the addition of the larger K ions into the structure, in contrast to the case when Na was added to β-LiAsSe₂. The red dashed curve is a theoretical $\chi_{\text{eff}}^{(2)}$ versus bandgap energy of the samples, ⁴³ which is given by

$$\chi_{\rm eff}^{(2)} = a/E^{1.5} \tag{2}$$

where a is scaling parameter to fit our result except for the γ -NaAsSe₂. For the three selenides, it is interesting to note that the experimental $\chi_{\rm eff}^{(2)}$ vs bandgap does not precisely follow the nominal trend represented by equation 2, but shows a constant or even slightly increasing $\chi_{\rm eff}^{(2)}$ with bandgap as indicated by the solid line in Figure 11a. We believe that this might be due to the opposing effect of the larger size of cation which is not quite large enough (based on the hypothesis of Song *et al*) to yield an increase in $\chi_{\rm eff}^{(2)}$. The dispersion curves for the refractive indices are shown in Figure S17 and exhibit a large birefringence of $\Delta n = 0.25$ at 0.78 eV which corresponds to 1580 nm (moderate birefringence $\Delta n = 0.04 - 0.1$), suggesting that these compounds may not be phase matchable up to 3 eV. ¹⁹

Structurally, the modulation of the SHG response from the cooperative effect of the $^{1}/_{\infty}[AQ_{2}^{-}]$ chains can be attributed to the distorted octahedron of the alkali metal coordination and the As...Se inter-chain interactions in all of the three structure types β -LiAsSe₂, γ -NaAsSe₂, and KAsSe₂. As mentioned above, the interchain interaction is the weakest in Na_{1-x}K_xAsSe₂ (x = 0.8, 0.65, and 0.5), which therefore has the lowest SHG response.

3.4.3 Laser-induced damage threshold

To assess the LIDT in these materials, the SHG counts of the reference and the samples at $d = 25 - 53 \mu m$ were measured as a function of the laser input intensity at 1580 nm. The SHG counts are expected to increase with the intensity according to the square-power law as

$$I_{SHG} = aI^2 \tag{3}$$

where I is the fundamental intensity, I_{SHG} is the SHG intensity, and a is a proportionality constant that is dependent on $\chi^{(2)}$. However, we found that the fundamental light started to undergo depletion with increasing I owing to three-photon absorption (3PA), as evidenced by the gradual deviation from the solid red line (Eq. 3) for each plot in Figure 11(b). The effect of 3PA can be incorporated via

$$I_{SHG} = aI_{3PA}^2 \text{ with } I_{3PA} = \frac{I}{(1+2\gamma dI^2)^{1/2}}$$
 (4)

where I_{3PA} is the input intensity modified by 3PA, γ is the 3PA coefficient,⁴⁴ and d = 25 - 53 µm for our reflection geometry.²⁷ The red dashed traces in Figure 11(b) correspond to the best fits to the data using Eq. 4 to obtain the 3PA coefficients of γ -NaAsSe₂ and Na_{0.2}K_{0.8}AsSe₂. The LIDT value is the onset point of 3PA i.e. the linear part of the curve. Figure 11b shows that the LIDT of γ -NaAsSe₂ (approximately 270 MW/cm²) was lower than that of Na_{0.2}K_{0.8}AsSe₂ (approximately 577 MW/cm²). Na_{0.2}K_{0.8}AsSe₂ showed a higher LIDT than AgGaSe₂ (approximately 230 MW/cm²). The obtained LIDT from powder AgGaSe₂ is comparable to the value obtained by single crystal AgGaSe₂ (139±6 MW/cm²).⁴⁵ Among all the compounds, Na_{0.1}K_{0.9}AsS₂ had the highest LIDT value of approximately 1170 MW/cm², which was approximately twice that of Na_{0.2}K_{0.8}AsSe₂. It is interesting to note that the bandgaps for the two compounds differ only by 0.11

eV, indicating that the bandgap might not be the only parameter that affects the LIDT as explained below The 3PA coefficient γ obtained from Eq. 4 also offers insight into the laser damage susceptibility of materials from 3PA. The higher the γ value is, the more likely is the material to be susceptible to laser damage from 3PA. The large 3PA coefficient $(4.75 \times 10^{-4} \text{ cm}^3/\text{MW}^2)$ of γ -NaAsSe₂ is most likely due to its low bandgap energy (E_g) as evident from the strong inverse relation $\gamma \propto 1/(E_g)^{6.5}$. When $(E_g)^{6.5}$ is most likely due to its larger bandgap energy ($(E_g)^{6.5}$) as a much smaller 3PA coefficient $(2.31 \times 10^{-5} \text{ cm}^3/\text{MW}^2)$ because of its larger bandgap, together with electronic band parameters for less probable 3PA, such as dipole matric elements and band curvatures specific to the sulfide. Table 3 summarizers the $\chi_{\text{eff}}^{(2)}$, LIDT and γ values of all reported compounds. Figure S18 shows the logarithmic plots from which the 3PA coefficients (γ) were obtained for all five compounds. In fact, 3PA is the dominant mechanism for the optical breakdown of compounds at intense excitation levels. Therefore, although Na_{0.2}K_{0.8}AsSe₂ and Na_{0.1}K_{0.9}AsS₂ possess relatively lower $\chi^{(2)}$ values, they are expected to perform better for high-power NLO applications.

3.6 Conclusions

The substitution limit of $Na_{1-x}K_xAsQ_2$ in the noncentrosymmetric structure is x = 0.5 forming $Na_{0.5}K_{0.5}AsSe_2$ in the selenides and a narrow substitution limit of x = 0.9 forming $Na_{0.1}K_{0.9}AsS_2$ in the sulfides. The K octahedra are also significantly distorted which plays a role tuning the $1/\infty[AQ_2]$ chain conformation compared to the Na octahedra in γ-NaAsSe₂. The addition of the larger-sized K atoms weakens the inter-chain As...Se interactions, resulting in wider bandgaps and lower melting points. These weakened interactions also significantly modify the electronic structure of these low-dimensional materials by increasing their bandgaps. The experimentally obtained $\chi_{\rm eff}^{(2)}=37~{\rm pm/V}$ for Na_{0.2}K_{0.8}AsSe₂ and 38 pm/V for $Na_{0.1}K_{0.9}AsS_2$ is lower than that of γ -NaAsSe₂, for which $\chi_{eff}^{(2)} = 148$ pm/V. However, $Na_{0.2}K_{0.8}AsSe_2$ has a higher LIDT of 577 MW/cm² than that of γ-NaAsSe₂. Table 5 summarizes the details of all reported AAsQ2 compounds. Among the compounds studied in this paper, Na_{0.1}K_{0.9}AsS2 has the highest LIDT and a $\chi_{eff}^{(2)}$ comparable to that of Na_{0.2}K_{0.8}AsSe₂ and AgGaSe₂. The electronic band structure of Na_{0.5}K_{0.5}AsSe₂ shows a relatively flat VB and high density of states similar to that of γ-NaAsSe₂; however, effective mass calculations suggest that γ-NaAsSe₂ has a greater electronic anisotropy. The hypothesis of Song et al that a large density of states contributes to a large $\chi^{(2)}$ appears to be valid up to a certain interchain distance and chain conformation in these compounds. These results offer both experimental and theoretical insights in the design of new low dimensional materials for NLO applications.

Associated Content

Supporting Information

Experimental methods and physical property measurements; X-ray crystallographic tables of atomic coordinates, displacement parameters, selected bond lengths, and bond angles of $Na_{0.2}K_{0.8}AsSe_2$, $Na_{0.35}K_{0.65}AsSe_2$, $Na_{0.5}K_{0.65}AsSe_2$ and, and $Na_{0.1}K_{0.9}AsS_2$; figures of PXRD patterns from all materials produced; energy dispersive spectroscopy data, powder XRD before and after DTA of $Na_{0.2}K_{0.8}AsSe_2$, $Na_{0.35}K_{0.65}AsSe_2$, $Na_{0.5}K_{0.5}AsSe_2$, $Na_{0.1}K_{0.9}AsS_2$; optical absorption data for all materials produced; particle size dependence of all produced compounds; band structure of $Na_{0.25}K_{0.75}AsSe_2$; SHG intensity of all produced compounds at $\lambda = 1580$ nm; theoretical refractive index of $Na_{0.5}K_{0.5}AsSe_2$; and plots with 3PA coefficient for all produced compounds.

CSD number for $Na_{0.1}K_{0.9}AsS_2$: 2100718

CSD number for Na_{0.2}K_{0.8}AsSe₂: 2100720

CSD number for Na_{0.35}K_{0.65}AsSe₂: 2100719

CSD number for Na_{0.5}K_{0.5}AsSe₂: 2100721

Author Information

Corresponding author: Mercouri G. Kanatzidis*

E-mail: m-kanatzidis@northwestern.edu

Note: The authors declare no competing financial interest.

Acknowledgements

M.G.K., V.G., A.K.I, and B.M.O. acknowledge the Air Force Office of Scientific Research Grant number FA9550-18-S-0003. The IMSERC PCM facility at Northwestern University used in this work received support from the Soft and Hybrid Nanotechnology Experimental (SHyNE) Resource (NSF ECCS-2025633), and Northwestern University. The computational work by J.M.R and M.J.W. was supported by the National Science Foundation (NSF) Grant No. DMR-2011208, and that by C.W. and S.H. partially supported by the Department of Energy, Office of Science Basic Energy Sciences under grant DE-SC0014520, DOE Office of Science. Access to facilities for high-performance computing resources at Northwestern University is acknowledged. J.I.J. acknowledges the support of the Basic Science Research Programs (2020R1F1A1069646 and 2021R1A2C2013625) through the National Research Foundation of Korea (NRF), funded by the Korean government. The authors would like to thank Dr. Daniel G. Chica and Dr. Vladislav Klepov for useful discussions and productive conversations.

References

- 1. Chung, I.; Kanatzidis, M. G., Metal Chalcogenides: A Rich Source of Nonlinear Optical Materials. *Chem. Mater.* **2013**, *26* (1), 849-869.
- 2. Nikogosyan, D. N., *Nonlinear Optical Crystals: A Complete Survey*. 1 ed.; Springer: New York, NY, **2005**; p XII, 428.

- 3. Boyd, R. W., *Nonlinear Optics*, Academic Press 3rd Edition. **2008**; p 1-613.
- 4. Luo, X.; Li, Z.; Guo, Y.; Yao, J.; Wu, Y., Recent progress on new infrared nonlinear optical materials with application prospect. *J. Solid State Chem.* **2019**, *270*, 674-687.
- 5. Pushkarsky, M. B.; Webber, M. E.; Macdonald, T.; Patel, C. K. N., High-sensitivity, high-selectivity detection of chemical warfare agents. *Appl Phys Lett* **2006**, *88* (4), 044103 1-3.
- 6. Pushkarsky, M.; Tsekoun, A.; Dunayevskiy, I. G.; Go, R.; Patel, C. K. N., Sub-parts-per-billion level detection of NO₂ using room-temperature quantum cascade lasers. *Proc. Natl. Acad. Sci.* **2006**, *103* (29), 10846-10849.
- 7. Dorn, R.; Baums, D.; Kersten, P.; Regener, R., Nonlinear Optical-Materials for Integrated-Optics Telecommunications and Sensors. *Adv. Mater.* **1992**, *4* (7-8), 464-473.
- 8. Eggleton, B. J.; Luther-Davies, B.; Richardson, K., Chalcogenide photonics. *Nature Photonics* **2011**, *5* (3), 141-148.
- 9. Schunemann, P. G.; Schepler, K. L.; Budni, P. A., Nonlinear frequency conversion performance of AgGaSe₂, ZnGeP₂, and CdGeAs₂. *Mrs Bull* **1998**, *23* (7), 45-49.
- 10. Liang, F.; Kang, L.; Lin, Z.; Wu, Y., Mid-Infrared Nonlinear Optical Materials Based on Metal Chalcogenides: Structure–Property Relationship. *Cryst. Growth & Design* **2017**, *17* (4), 2254-2289.
- 11. Lin, H.; Wei, W.-B.; Chen, H.; Wu, X.-T.; Zhu, Q.-L., Rational design of infrared nonlinear optical chalcogenides by chemical substitution. *Coord. Chem. Rev.* **2020**, *406*, 213150 1-24.
- 12. Bera, T. K.; Jang, J. I.; Song, J.-H.; Malliakas, C. D.; Freeman, A. J.; Ketterson, J. B.; Kanatzidis, M. G., Soluble Semiconductors AAsSe₂ (A=Li, Na) with a Direct-Band-Gap and Strong Second Harmonic Generation: A Combined Experimental and Theoretical Study. *J. Am. Chem. Soc.* **2010**, *132*, 3484–3495.
- 13. Chung, I.; Jang, J. I.; Malliakas, C. D.; Ketterson, J. B.; Kanatzidis, M. G., Strongly Nonlinear Optical Glass Fibers from Noncentrosymmetric Phase-Change Chalcogenide Materials. *J. Am. Chem. Soc.* **2010**, *132*, 384–389.
- 14. Haynes, A. S.; Saouma, F. O.; Otieno, C. O.; Clark, D. J.; Shoemaker, D. P.; Jang, J. I.; Kanatzidis, M. G., Phase-Change Behavior and Nonlinear Optical Second and Third Harmonic Generation of the One-Dimensional $K_{(1-x)}Cs_xPSe_6$ and Metastable β -CsPSe₆. *Chem. Mater.* **2015**, *27* (5), 1837-1846.
- 15. Song, J.-H.; Freeman, A. J.; Bera, T. K.; Chung, I.; Kanatzidis, M. G., First-principles prediction of an enhanced optical second-harmonic susceptibility of low-dimensional alkali-metal chalcogenides. *Phys. Rev. B* **2009**, *79* (24), 245203 1-6.
- 16. Chung, I.; Song, J.-H.; Jang, J. I.; Freeman, A. J.; Kanatzidis, M. G., Na₂Ge₂Se₅: A highly nonlinear optical material. *J. Solid State Chem.* **2012**, *195*, 161-165.
- 17. Bera, T. K.; Song, J. H.; Freeman, A. J.; Jang, J. I.; Ketterson, J. B.; Kanatzidis, M. G., Soluble direct-band-gap semiconductors LiAsS₂ and NaAsS₂: large electronic structure effects from weak As...S interactions and strong nonlinear optical response. *Angew. Chem. Int. Ed. Engl.* **2008**, 47 (41), 7828-32.
- 18. Isaenko, L. I.; Yelisseyev, A. P., Recent studies of nonlinear chalcogenide crystals for the mid-IR. *Semiconductor Science and Technology* **2016**, *31* (12), 123001.
- 19. Kang, L.; Liang, F.; Jiang, X.; Lin, Z.; Chen, C., First-Principles Design and Simulations Promote the Development of Nonlinear Optical Crystals. *Acc. Chem. Res.* **2020**, *53* (1), 209-217.
- 20. Bi-Lian, N.; He-Gen, Z.; Jun-Quan, J.; Yi, L.; Yong-Fan, Z., Electronic Structure and Optical Properties of the Novel Nonlinear LiAsSe₂ Crystal. *Acta Phys. -Chim. Sin.* **2010**, *26* (11), 3052-3060.
- 21. Liao, J. H.; Varotsis, C.; Kanatzidis, M. G., Syntheses, Structures, and Properties of 6 Novel Alkali-Metal Tin Sulfides $K_2Sn_2S_8$, α -Rb₂Sn₂S₈, β -Rb₂Sn₂S₈, $K_2Sn_2S_5$, $Cs_2Sn_2S_6$, and Cs_2SnS_{14} . *Inorg. Chem.* **1993**, *32* (11), 2453-2462.
- 22. Mccarthy, T. J.; Kanatzidis, M. G., Use of Molten Alkali-Metal Polythiophosphate Fluxes for Synthesis at Intermediate Temperatures Isolation and Structural Characterization of $ABiP_2S_7$ (A = K, Rb). *Chem. Mater.* **1993**, *5* (8), 1061-1063.
- 23. Kresse, G.; Furthmüller, J., Efficient iterative schemes for ab initio total-energy calculations using a plane-wave basis set. *Phys. Rev. B* **1996**, *54*, 11169.
- 24. Romero, A. H.; Allan, D. C.; Amadon, B.; Antonius, G.; Applencourt, T.; Baguet, L.; Bieder, J.; Bottin, F.; Bouchet, J.; Bousquet, E.; Bruneval, F.; Brunin, G.; Caliste, D.; Côté, M.; Denier, J.;

- Dreyer, C.; Ghosez, P.; Giantomassi, M.; Gillet, Y.; Gingras, O.; Hamann, D. R.; Hautier, G.; Jollet, F.; Jomard, G.; Martin, A.; Miranda, H. P. C.; Naccarato, F.; Petretto, G.; Pike, N. A.; Planes, V.; Prokhorenko, S.; Rangel, T.; Ricci, F.; Rignanese, G.-M.; Royo, M.; Stengel, M.; Torrent, M.; Setten, M. J. v.; Troeye, B. V.; Verstraete, M. J.; Wiktor, J.; Zwanziger, J. W.; Gonze, X., ABINIT: Overview, and focus on selected capabilities. *J. Chem. Phys.* **2020**, *152*, 124102.
- 25. Larsen, A. H.; Mortensen, J. J.; Blomqvist, J.; Castelli, I. E.; Christensen, R.; Dułak, M.; Friis, J.; Groves, M. N.; Hammer, B.; Hargus, C.; Hermes, E. D.; Jennings, P. C.; Jensen, P. B.; Kermode, J.; Kitchin, J. R.; Kolsbjerg, E. L.; Kubal, J.; Kaasbjerg, K.; Lysgaard, S.; Maronsson, J. B.; Maxson, T.; Olsen, T.; Pastewka, L.; Peterson, A.; Rostgaard, C.; Schiøtz, J.; Schütt, O.; Strange, M.; Thygesen, K. S.; Vegge, T.; Vilhelmsen, L.; Walter, M.; Zeng, Z.; Jacobsen, K. W., The Atomic Simulation Environment—A Python library for working with atoms. *J. Phys.: Condens. Matter* **2017**, *29*, 273002.
- 26. Holzwarth, N. A. W., Updated comments on projector augmented wave (PAW) implementations within various electronic structure code packages. *Comp. Phys. Comm.* **2019**, *243*, 25-29.
- 27. Zhang, J. H.; Clark, D. J.; Brant, J. A.; Rosmus, K. A.; Grima, P.; Lekse, J. W.; Jang, J. I.; Aitken, J. A., alpha-Li₂ZnGeS₄: A Wide-Bandgap Diamond-like Semiconductor with Excellent Balance between Laser-Induced Damage Threshold and Second Harmonic Generation Response. *Chem. Mater.* **2020**, *32* (20), 8947-8955.
- 28. Sheldrick, W. S.; Hatjsle, H.-J., Zur Kenntnis von Alkalimetaselenoarseniten Darstellung und Kristallstrukturen von MAsSe₂, (M = K, Rb, Cs). *Z. Anorg. Allg. Chem.* **1988**, *561*, 139-148.
- 29. Eisenmann, B.; Schafer, H., Selenoarsenites and Telluroarsenites, Telluroantimonites, and Tellurobismutites. *Z Anorg Allg Chem* **1979**, *456* (9), 87-94.
- 30. Kapon, M.; Reisner, G. M., On the structure of KAsSe₂. Acta Cryst. 1989, C45, 2029.
- 31. Shannon, R. D., Revised Effective Ionic Radii and Systematic Studies of Interatomie Distances in Halides and Chaleogenides. *Acta Cryst.* **1976**, *A32*, 751-767.
- 32. Alonso, J. A.; Martínez-Lope, M. J.; Casais, M. T.; Fernández-Díaz, M. T., Evolution of the Jahn-Teller Distortion of MnO6 Octahedra in RMnO3 Perovskites (R = Pr, Nd, Dy, Tb, Ho, Er, Y): A Neutron Diffraction Study. *Inorg. Chem.* **2000**, *39*, 917-923.
- 33. Brehm, J. A.; Young, S. M.; Zheng, F.; Rappe, A. M., First-principles calculation of the bulk photovoltaic effect in the polar compounds LiAsS₂, LiAsSe₂, and NaAsSe₂. *J. Chem. Phys.* **2014**, *141* (20), 204704.
- 34. Perdew, J. P.; Yang, W.; Burke, K.; Yang, Z.; Gross, E. K. U. S., M.; Scuseria, G. E.; Henderson, T. M.; Zhang, I. Y.; Ruzsinszky, A.; Peng, H.; Sun, J.; Trushin, E.; Görling, A., Understanding band gaps of solids in generalized Kohn–Sham theory. *Proc. Natl. Acad. Sci.* **2017**, *114* (11), 2801-2806.
- 35. Tauc, J.; Grigorovici, R.; Vancu, A., Optical Properties And Electronic Structure of Amorphous Germanium. *Phys. Status Solidi B* **1966**, *15*, 627–637.
- 36. Hadar, I.; Hu, X. B.; Luo, Z. Z.; Dravid, V. P.; Kanatzidis, M. G., Nonlinear Band Gap Tunability in Selenium Tellurium Alloys and Its Utilization in Solar Cells. *ACS Energy Lett.* **2019**, *4* (9), 2137-2143.
- 37. Rosmus, K. A.; Brant, J. A.; Wisneski, S. D.; Clark, D. J.; Kim, Y. S.; Jang, J. I.; Brunetta, C. D.; Zhang, J. H.; Srnec, M. N.; Aitken, J. A., Optical nonlinearity in Cu(2)CdSnS(4) and alpha/beta-Cu(2)ZnSiS(4): diamond-like semiconductors with high laser-damage thresholds. *Inorg Chem* **2014**, *53* (15), 7809-11.
- 38. Zhang, J.-H.; Clark, D. J.; Weiland, A.; Stoyko, S. S.; Kim, Y. S.; Jang, J. I.; Aitken, J. A., Li2CdGeSe4and Li2CdSnSe4: biaxial nonlinear optical materials with strong infrared second-order responses and laser-induced damage thresholds influenced by photoluminescence. *Inorganic Chemistry Frontiers* **2017**, *4* (9), 1472-1484.
- 39. Zhang, W.; Yu, H.; Wu, H.; Halasyamani, P. S., Phase-Matching in Nonlinear Optical Compounds: A Materials Perspective. *Chem. Mater.* **2017**, *29* (7), 2655-2668.
- 40. Kurtz, S. K.; Perry, T. T., A Powder Technique for Evaluation of Nonlinear Optical Materials. *J Appl Phys* **1968**, *39* (8), 3798-3813.

- 41. Mattiucci, N.; D'Aguanno, G.; Scalora, M.; Bloemer, M., Coherence length for second-harmonic generation in nonlinear, one-dimensional, finite, multilayered structures. *J. Opt. Soc. Am. B* **2007**, *24* (4), 877-886.
- 42. Brant, J. A.; Clark, D. J.; Kim, Y. S.; Jang, J. I.; Weiland, A.; Aitken, J. A., Outstanding Laser Damage Threshold in Li₂MnGeS₄ and Tunable Optical Nonlinearity in Diamond-Like Semiconductors. *Inorg. Chem.* **2015**, *54* (6), 2809-2819.
- 43. Jackson, A. G.; Ohmar, M. C.; LeClair, S. R., Relationship of the second order nonlinear optical coefficient to energy gap in inorganic non-centrosymmetric crystals. *Infrared Physics & Technology* **1997**, *38*, 233-244.
- 44. He, J.; Qu, Y. L.; Li, H. P.; Mi, J.; Ji, W., Three-photon absorption in ZnO and ZnS crystals. *Opt Express* **2005**, *13* (23), 9235-9247.
- 45. Andreev, Y. M.; Badikov, V. V.; Geiko, P. P.; Grechin, S. G.; Efimenko, V. V.; Efimenko, T. D.; Panyutin, V. L.; Tikhomirov, A. A.; Shaiduko, A. V., Second harmonic generation of TEA CO₂ laser radiation in LiInSe₂. *Atmos. Oceanic Opt.* **2004**, *17*, 115-120.
- 46. Clark, D. J.; Stoumpos, C. C.; Saouma, F. O.; Kanatzidis, M. G.; Jang, J. I., Polarization-selective three-photon absorption and subsequent photoluminescence in CsPbBr₃ single crystal at room temperature. *Physical Review B* **2016**, *93* (19), 195202.
- 47. Cho, J. B.; Jung, G.; Kim, K.; Kim, J.; Hong, S.-K.; Song, J. -H.; Jang, J. I., Highly Asymmetric Optical Properties of β -Ga₂O₃ as Probed by Linear and Nonlinear Optical Excitation Spectroscopy. *J. Phys. Chem. C* **2021**, *125*, 1432-1440.

Table 1. Crystal data and structure refinement for $Na_{1-x}K_xAsSe_2$ ($x=0.8,\,0.65$ and 0.5) and $Na_{0.1}K_{0.9}AsS_2$ at 293 K.

Empirical formula	Na _{0.2} K _{0.8} AsSe ₂	Na _{0.35} K _{0.65} AsSe ₂ Na _{0.5} K _{0.5} AsSe ₂		Na _{0.1} K _{0.9} AsS ₂				
Formula weight	1074.87	1065.45	1055.54	706.12				
Wavelength	0.71073 Å							
Crystal system	Monoclinic							
Space group	Cc							
	a = 7.7400(15) Å, $\alpha = 90^{\circ}$	a = 7.7642(16) Å, $\alpha = 90^{\circ}$	$a = 7.7350(15) \text{ Å}, \alpha$ = 90°	$a = 7.5060(15) \text{ Å}, \alpha$ = 90°				
Unit cell	$b = 10.310(2) \text{ Å}, \beta$	b = 10.164(2) Å,	$b = 10.010(2) \text{ Å}, \beta =$	$b = 9.987(2) \text{ Å}, \beta =$				
dimensions	$= 106.10(3)^{\circ}$	$\beta = 105.87(3)^{\circ}$	104.74(3)°	107.08(3)°				
	c = 12.490(3) Å,	c = 12.403(3) Å,	$c = 12.281(3) \text{ Å}, \gamma =$	$c = 11.908(2) \text{ Å}, \gamma$				
	$\gamma = 90^{\circ}$	$\gamma = 90^{\circ}$	90°	= 90°				
Volume	957.6(4) Å ³	941.5(4) Å ³	919.6(3) Å ³	853.3(3) Å ³				
Z	,		2					
Density (calculated)	3.728 g/cm ³	3.758 g/cm ³	3.812 g/cm ³	2.748 g/cm ³				
Absorption coefficient	22.810 mm ⁻¹	23.084 mm ⁻¹	23.508 mm ⁻¹	9.601 mm ⁻¹				
F(000)	947	938	928	666				
Crystal size	0.14 x 0.14 x 0.23 mm ³	0.2 x 0.4 x 0.5 mm ³	0.01 x 0.13 x 0.2 mm ³	0.09 x 0.13 x 0.19 mm ³				
θ range for data collection	3.377 to 33.397°	3.385 to 33.386°	3.400 to 33.306°	3.496 to 33.408°				
	-11<=h<=11,	-11<=h<=11,	-11<=h<=11,	-11<=h<=11,				
Index ranges	0<=k<=15,	0<=k<=15,	0<=k<=15,	0<=k<=15,				
	-19<=1<=19	0<=1<=19	-18<=l<=18	-18<=1<=18				
Reflections collected	3097	1812	3249	3130				
Independent reflections	3097	1812	3249	3130				
Completeness to $\theta = 25.242^{\circ}$	100%	100%	99.5%	100%				
Refinement	Full-matrix least-	Full-matrix least-	Full-matrix least-	Full-matrix least-				
method	squares on F ²	squares on F ²	squares on F ²	squares on F ²				
Data / restraints / parameters	309////		3249 / 0 / 71	3130 / 0 / 75				
Goodness-of-fit	0.849	0.961	1.039	0.759				
Final R indices [I	$R_{obs} = 0.0845,$	$R_{obs} = 0.0631,$	$R_{obs} = 0.0361, wR_{obs}$	$R_{obs} = 0.0511,$				
> 2σ(I)]	$wR_{obs} = 0.2045$	$wR_{obs} = 0.1337$	= 0.0892	$wR_{obs} = 0.1163$				
R indices [all	$R_{all} = 0.2390,$	$R_{all} = 0.1115,$	$R_{all} = 0.0535$, $wR_{all} =$	$R_{all} = 0.1861, wR_{all}$				
data]	$wR_{all} = 0.2851$	$wR_{all} = 0.1557$	0.1007	= 0.1407				
Largest diff.	2.167 and -1.720	1.529 and -1.361	0.958 and -0.958	0.795 and -0.865				
peak and hole	$e \cdot \mathring{A}^{-3}$ $e \cdot \mathring{A}^{-3}$		e·Å-³	e∙Å ⁻³				

Table 2. Atomic coordinates ($\times 10^4$) and equivalent isotropic displacement parameters ($\mathring{A}^{2\times}10^3$) for Na_{0.5}K_{0.5}AsSe₂ at 293(2) K with estimated standard deviations in parentheses.

Label	Wyckoff sites	X	y	z	Occupancy	Ueq*	
K(1)	4a	6684(8)	2229(2)	2499(4)	1	37(1)	
Na(2)	4a	0	115(5)	0	1	36(1)	
As(1)	4a	454(7)	4036(2)	568(4)	1	39(1)	
As(2)	4a	2344(7)	1907(2)	2981(4)	1	32(1)	
Se(1)	4a	175(7)	267(2)	2539(4)	1	37(1)	
Se(2)	4a	547(7)	3920(1)	2578(4)	1	35(1)	
Se(3)	4a	2644(7)	2565(2)	329(4)	1	40(1)	
Se(4)	4a	2707(7)	2294(2)	4998(4)	1	44(1)	

 $^{^*}U_{eq}$ is defined as one-third of the trace of the orthogonalized U_{ij} tensor.

Table 3. Experimental NLO properties of the title compounds and the reference.

	AgGaSe ₂	$Na_{0.2}K_{0.8}AsSe_2$	Na _{0.35} K _{0.65} AsSe ₂	$Na_{0.5}K_{0.5}AsSe_2$	$Na_{0.1}K_{0.9}AsS_2$	γ-NaAsSe ₂
E_g (eV)	1.79	2.07	2.01	1.78	2.18	1.75
X ⁽²⁾	56	37±4	28±2	33±3	38±4	148±11
(pm/V)						
γ (×10 ⁻⁴	5.02	0.97	1.63	1.57	0.23	4.75
cm ³ /MW ²)						
LIDT	230	577	458	437	1177	270
(MW/cm ²)						

 $\textbf{Table 4}. \ \ Calculated \ effective \ mass \ of \ holes \ and \ electrons \ in \ KAsSe_2, \ Na_{0.25}K_{0.75}AsSe_2, \ Na_{0.5}K_{0.5}AsSe_2 \ and \ \gamma-NaAsSe_2.$

Effective mass direction	KAsSe ₂	Na _{0.25} K _{0.75} AsSe ₂	$Na_{0.5}K_{0.5}AsSe_2$	γ-NaAsSe ₂
		Electrons		
a*	0.179 m_0	0.105 m_0	$0.098 \; m_0$	0.219 m_0
b*	0.154 m ₀	0.134 m ₀	0.126 m_0	0.517 m ₀
c*	0.238 m ₀	0.220 m ₀	$0.200 \; m_0$	4.961 m ₀
		Holes		
a*	0.820 m_0	0.880 m_0	$0.890 \; m_0$	1.360 m ₀
b*	0.522 m ₀	0.539 m ₀	0.559 m_0	2.159 m ₀
c*	0.715 m ₀	0.765 m ₀	0.812 m ₀	2.370 m ₀

 $m_0 = mass of free electron$

Table 5. Summary of the noncentrosymmetric AAs Q_2 compounds.

Material	Spac e Grou p	Bandg ap (eV)	Experime ntal $\chi_{\rm eff}^{(2)}$ (pm/V) (powder)	Theoreti cal max Xijk ⁽²⁾ (pm/V) Static	LIDT (MW/c m²)	Melti ng point (°C)	Crystallizi ng point (°C)	Referen ce
LiAsS ₂	Сс	1.60	10 xAgGaSe ₂	196.3	Not measure d	524	503	15, 17
Li _{0.6} Na _{0.4} As S ₂	Сс	1.88	30 xAgGaSe ₂	Not calculate d	Not measure d	480	460	17
β-LiAsSe ₂	Сс	1.11	Not measured	1673	Not measure d	455	416	12, 20
β- Li _{0.2} Na _{0.8} As Se ₂	Сс	1.57	55 xAgGaSe ₂	Not calculate d	Not measure d	440	410	12
γ- Li _{0.2} Na _{0.8} As Se ₂	Pc	1.72	65 xAgGaSe ₂	Not calculate d	Not measure d	440	410	12
γ-NaAsSe ₂	Pc	1.75 1.87 (Tauc method	75 xAgGaSe ₂ 148**	324.6	270**	444	413	This Work
Na _{0.5} K _{0.5} AsS e ₂	Сс	1.75*	33**	45.0	437	318	287	This work
Na _{0.35} K _{0.65} As Se ₂	Сс	2.01	28**	Not calculate d	458	316	271	This work
Na _{0.2} K _{0.8} AsS e ₂	Сс	2.07	37**	Not calculate d	577	316	264	This work
Na _{0.1} K _{0.9} AsS 2	Cc	2.18	38**	Not calculate d	1177	361	Not observed	This work

^{*} Compound contains impurity

** Experimental values obtained from equation 1

Figures

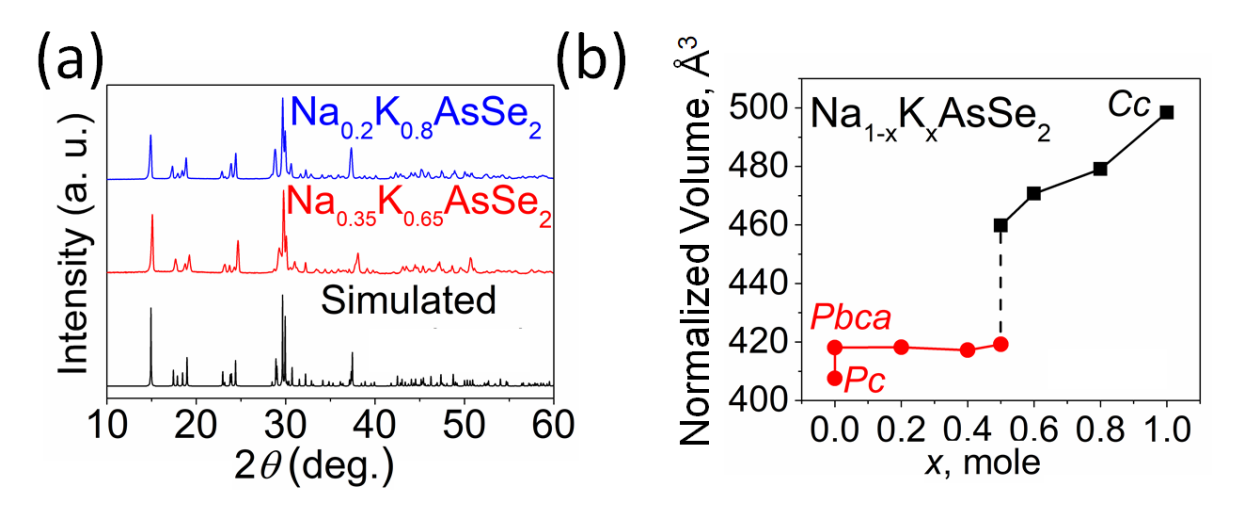


Figure 1. (a) Experimental powder XRD patterns of $Na_{0.35}K_{0.65}AsSe_2$ (red) and $Na_{0.2}K_{0.8}AsSe_2$ (blue) compared with the simulated pattern of $Na_{0.2}K_{0.8}AsSe_2$ obtained from single-crystal XRD. (b) Plot of normalized unit cell volume vs composition of $Na_{1-x}K_xAsSe_2$. Two distinct structural transitions are observed.

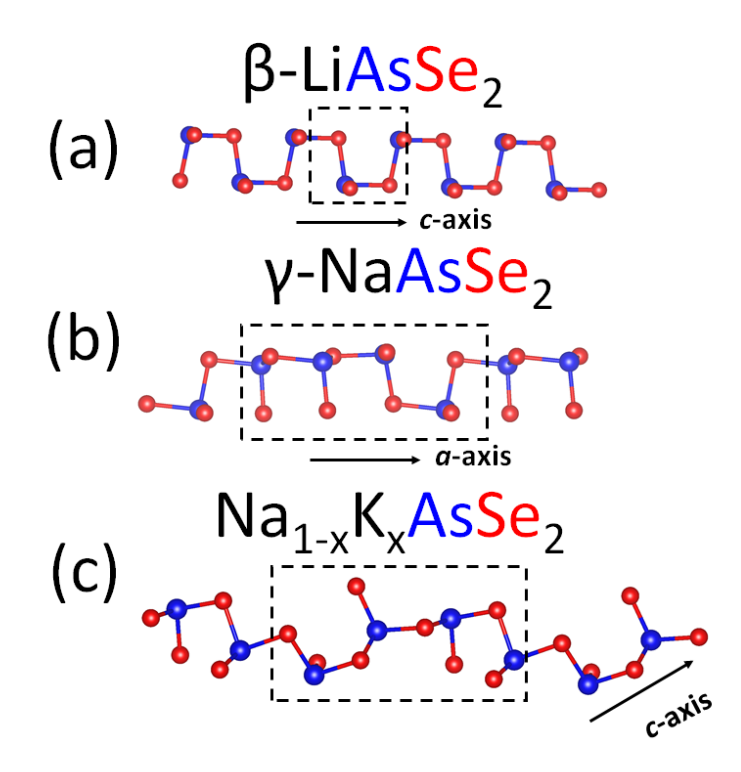


Figure 2. A comparison of the different conformations of the $^{1}/_{\infty}[AQ_{2}^{-}]$ chains in the structures of (a) β-LiAsSe₂, (b) γ-NaAsSe₂, and (c) Na_{1-x}K_xAsSe₂. The dotted boxes show the repeating units in the chain of each structure.

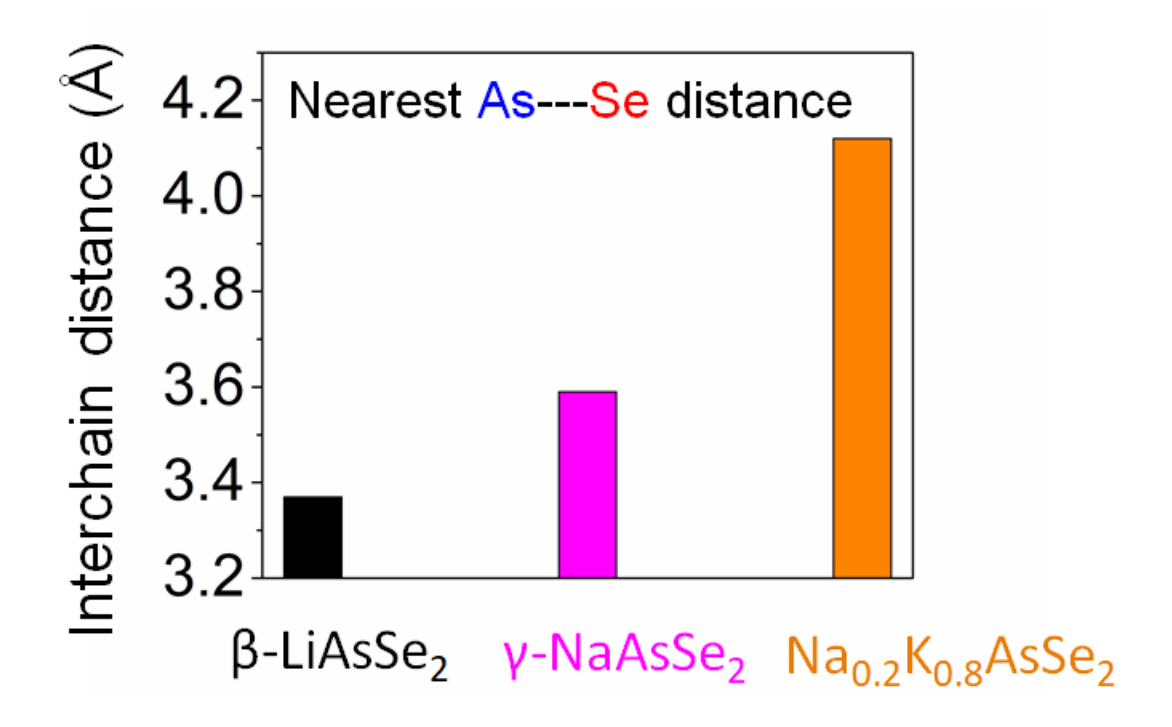


Figure 3. A comparison of the interchain distances of β -LiAsSe₂, γ -NaAsSe₂, and Na_{0.2}K_{0.8}AsSe₂.

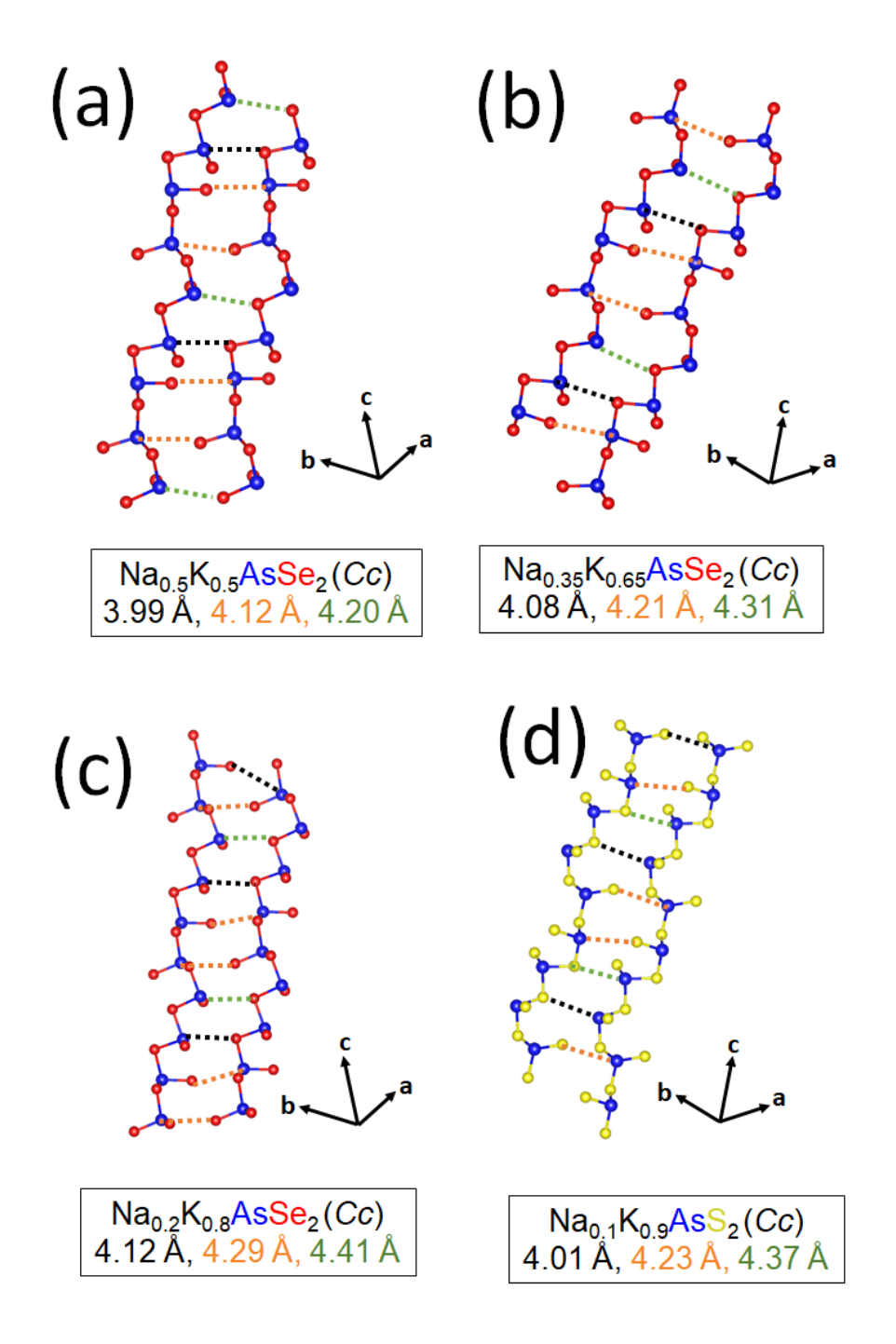


Figure 4. The interchain distances, which show an increase with increasing K substitution, of (a) $Na_{0.5}K_{0.5}AsSe_2$, (b) $Na_{0.35}K_{0.65}AsSe_2$, (c) $Na_{0.2}K_{0.8}AsSe_2$, and (d) $Na_{0.1}K_{0.9}AsS_2$.

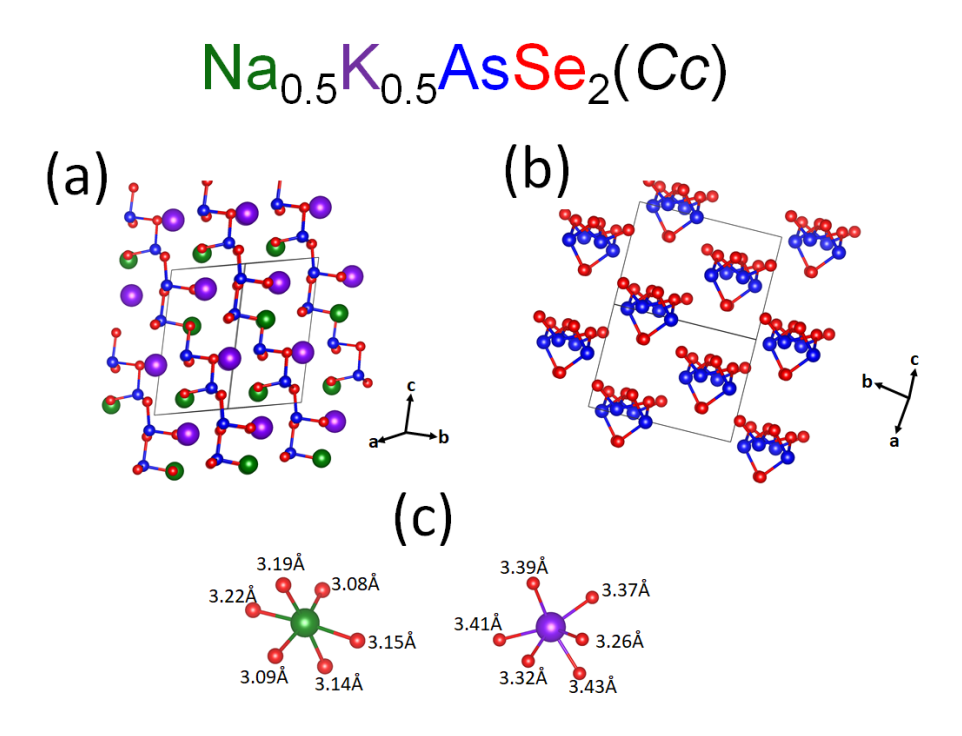


Figure 5. (a) The unit cell of $Na_{0.5}K_{0.5}AsSe_2$ showing the independent sites of Na (green) and K (purple); (b) the chain direction of $(^1/_{\infty})[AsSe_2^-]$ in $Na_{0.5}K_{0.5}AsSe_2$; (c) the bond lengths of the KSe₆ and NaSe₆ octahedra. The Na, K, and Se atoms are denoted in green, purple, and red, respectively.

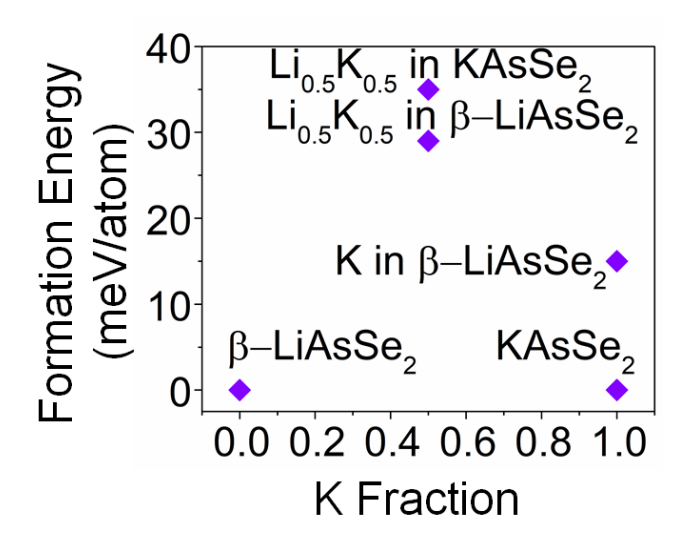


Figure 6. Calculated formation energy differences. β-LiAsSe₂ and KAsSe₂ are taken as the lowest-energy structures.

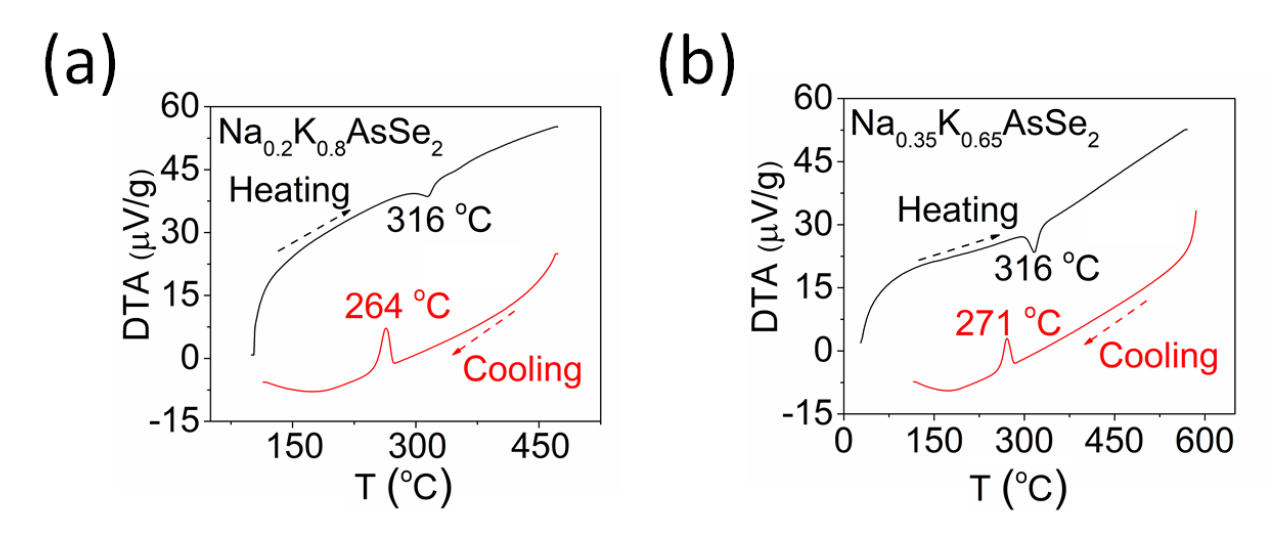


Figure 7. Differential thermal analysis of (a) $Na_{0.2}K_{0.8}AsSe_2$ and (b) $Na_{0.35}K_{0.65}AsSe_2$ showing the melting (T_m , endothermic) and crystallizing (T_c , exothermic) points.

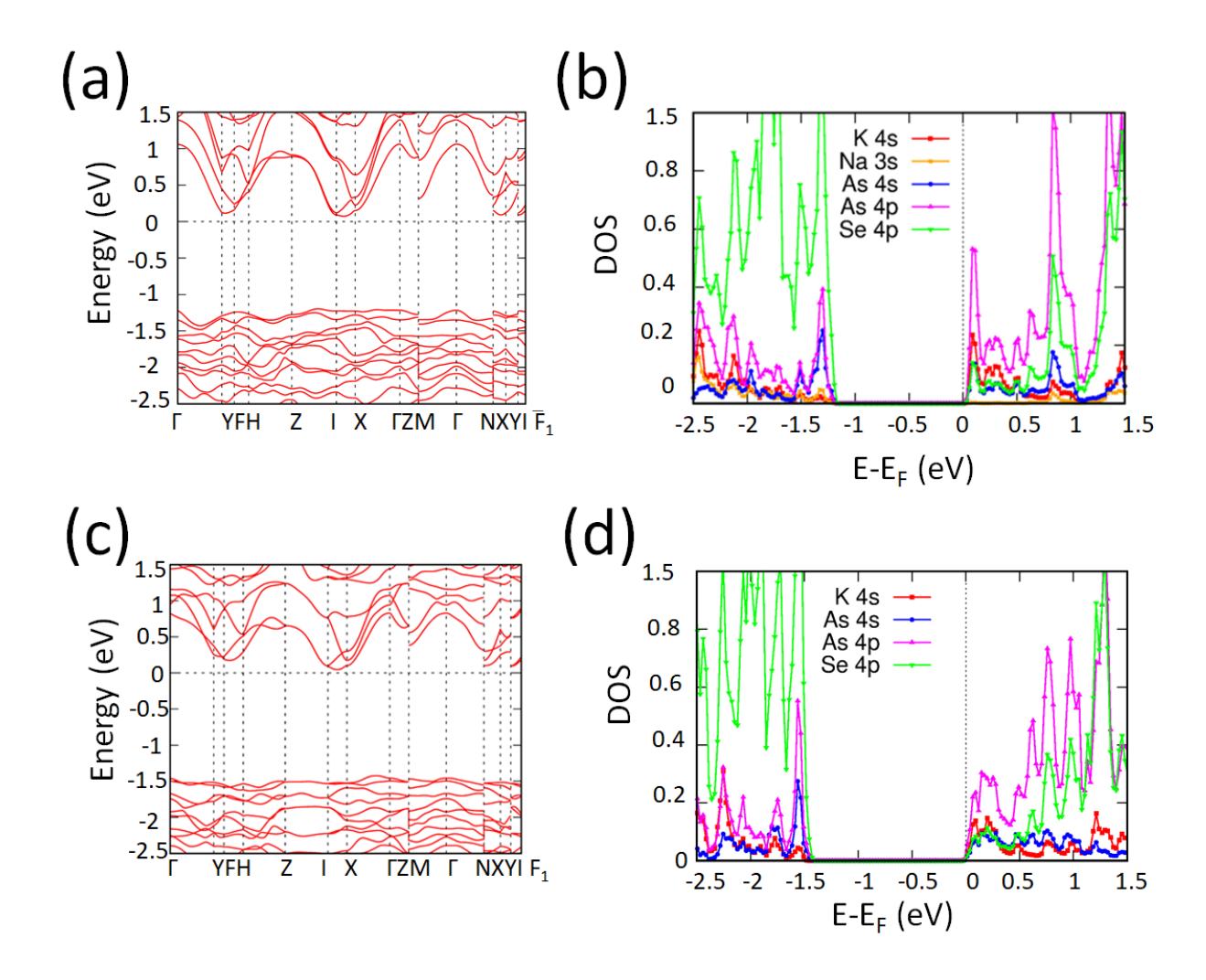


Figure 8. Calculated (a) band structure and (b) electronic density of states (DOS) of Na_{0.5}K_{0.5}AsSe₂, and (c) the band structure of KAsSe₂ and (d) its electronic density of states. The Fermi level E_F is set to the conduction band minimum.

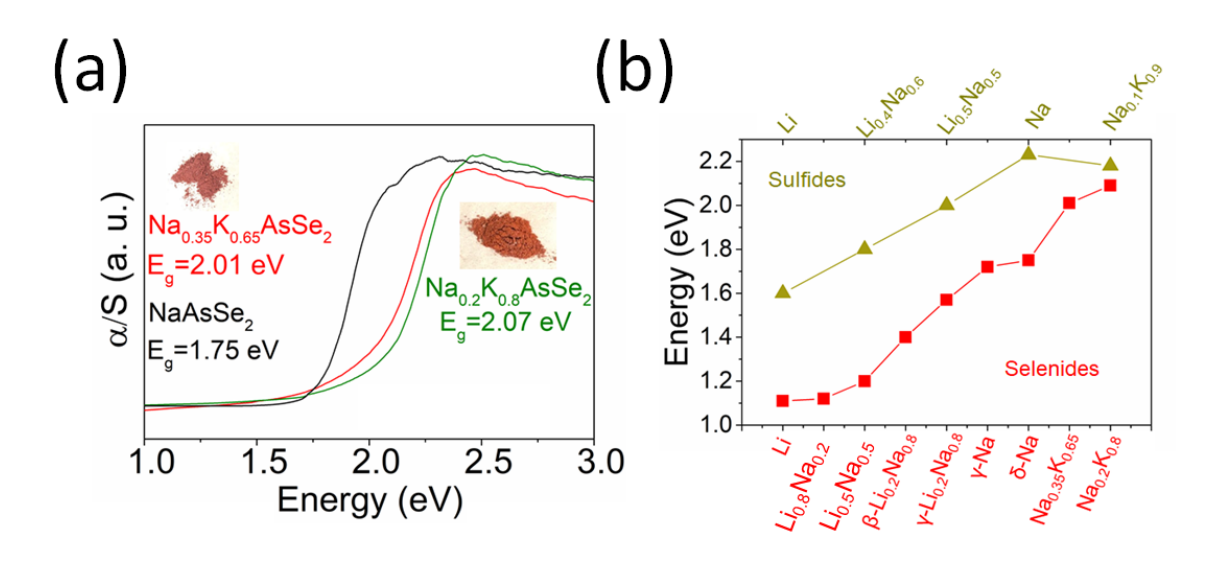


Figure 9. (a) UV-visible optical absorption spectra of Na_{0.2}K_{0.8}AsSe₂, Na_{0.35}K_{0.65}AsSe₂, and NaAsSe₂; (b) evolution of bandgap with composition from β-LiAsSe₂ to γ-NaAsSe₂ and Na_xK_{1-x}AsSe₂.

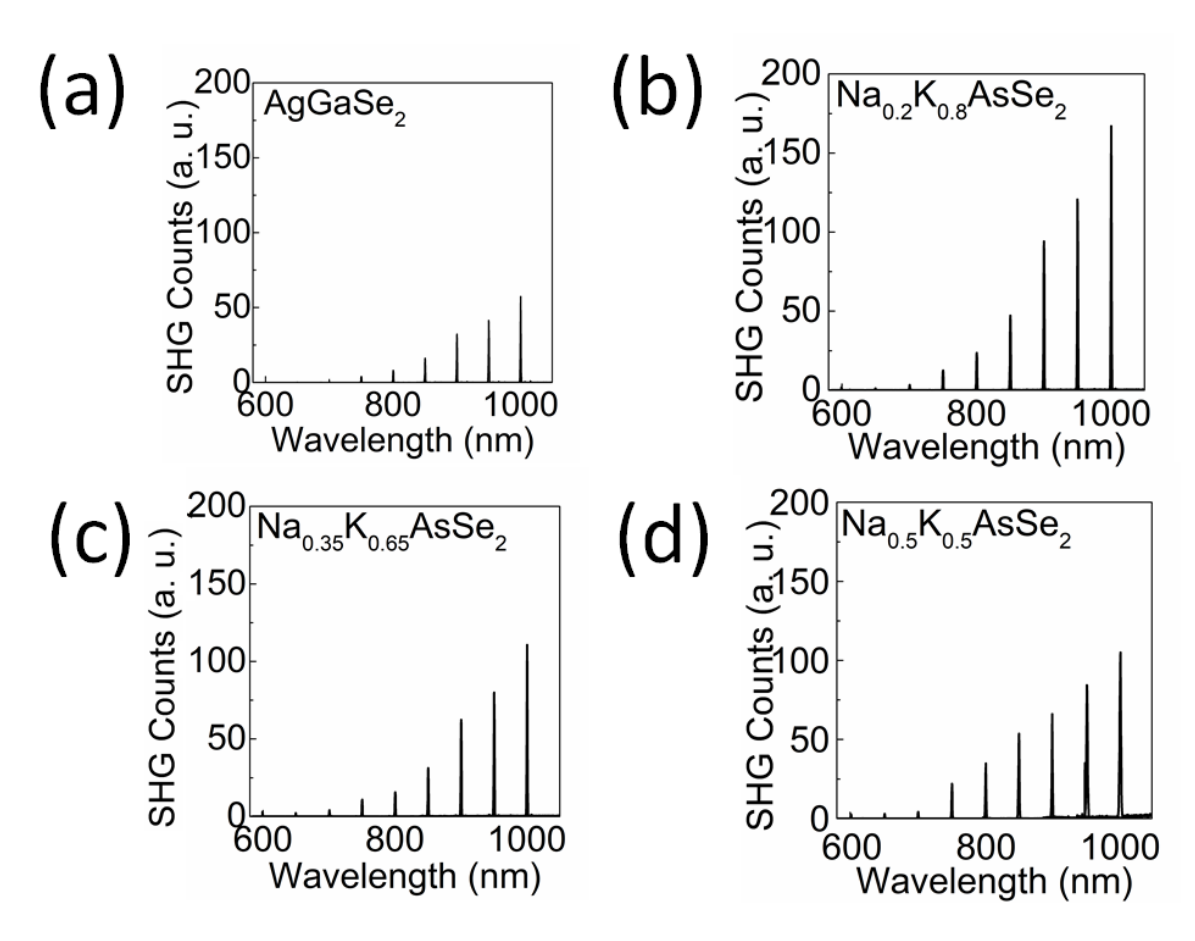


Figure 10. Broadband SHG intensity of (a) AgGaSe₂, (b) Na_{0.2}K_{0.8}AsSe₂, (c) Na_{0.35}K_{0.65}AsSe₂, and (d) Na_{0.5}K_{0.5}AsSe₂ for particle size $d = 25 - 53 \mu m$.

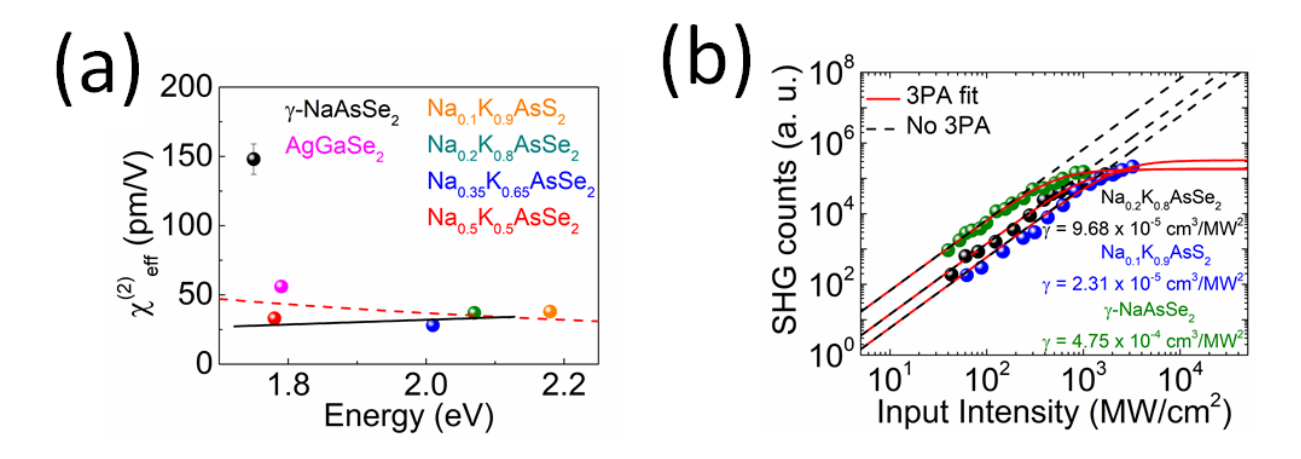


Figure 11. (a) Powder SHG measurements showing a comparison of the experimental $\chi_{eff}^{(2)}$ vs bandgap of Na_{0.2}K_{0.8}AsSe₂, Na_{0.35}K_{0.65}AsSe₂, Na_{0.5}K_{0.5}AsSe₂, and Na_{0.1}K_{0.9}AsS₂ compared with those of γ-NaAsSe₂ and AgGaSe₂. The dashed red curve indicates a theoretical $\chi_{eff}^{(2)}$ as a function of bandgap (eq. 2). The black line is the guide to the eye, showing minor but noticeable increase in $\chi_{eff}^{(2)}$ with increasing bandgap of the selenides. (b) Logarithmic plots of the SHG counts vs. input intensity at $\lambda = 1580$ nm for Na_{0.1}K_{0.9}AsS₂, Na_{0.2}K_{0.8}AsSe₂, and γ-NaAsSe₂. The solid red line in each plot corresponds to the square power law (eq. 3) for ideal SHG. The red dashed trace is a theoretical fit for each composition accounting for the presence of 3PA (eq. 4).

TOC Graphic

